Self-Coagulations of Mass and Energy in Laboratory Plasmas and Their Implications

Rui-Ji Tang , Shu-Xia Zhao * , Yu Tian

Posted Date: 10 April 2026

doi: 10.20944/preprints202604.0734.v1

Keywords: self-coagulation of mass and energy; physically and chemically ambi-polar type; Schrodinger equation; β decay; neutrino; asymmetry; spin orientation; photon model; inter-disciplinary work

 doi:10.20944/preprints202604.0734.v1

Article

Self-Coagulations of Mass and Energy in Laboratory Plasmas and Their Implications

Rui-Ji Tang [1], Shu-Xia Zhao [1,*] and Yu Tian [2]

[1] Key Laboratory of Material Modification by Laser, Ion, and Electron Beams (Ministry of Education), School of Physics, Dalian University of Technology, Dalian, 116024, China

[2] Experimental training center, Dalian University of Science and Technology, Dalian, 116052, China

* Correspondence: zhaonie@dlut.edu.cn

Abstract

In this article, the different types of self-coagulation discovered in the fluid simulations of inductively coupled plasma (abbreviated as ICP) at both the electronegative and electropositive cases are presented. Among these, the electronegative plasma sources include the Ar/O_2, Ar/Cl_2, and Ar/SF_6 ones, and the electropositive plasma source is the inertial argon plasma itself. The fluid simulation versions are not the same. Concretely, the Comsol software is used to simulate the Ar/O_2, Ar/Cl_2, Ar/SF_6, and the pure argon ICPs, and the self-written code of fluid model is used to simulate the pure argon ICP as well, but in a different framework of fluid design. The types of self-coagulation refined from these fluid simulations are the physically ambi-polar self-coagulation of ions, the chemically ambi-polar self-coagulation of ions, the mono-polar self-coagulation of electrons, and the non-polar self-coagulation of argon metastable atoms. It is noted these self-coagulations are based on the mass and found in the Comsol fluid simulations, and moreover the self-coagulation of thermal energy of electrons is also given and found in the self-written fluid code simulation. The self-coagulations of mass and energy found in the laboratory plasmas have significant implications on ambi-polar diffusion, the wave-particle duality, application of Schrodinger equation, the positive and reverse species pair, the β^- and β^+ decay, the spin orientations of neutrino and anti-neutrino, the symmetry and asymmetry, and the photon model. It is believed this interdisciplinary work of plasma physics with the quantum mechanics, the particle physics, the nuclear physics, and the optics are useful for us better understanding the mass and energy general dynamics. The self-coagulation definition constructed herein is reliable since it is validated in many circumstances, such as in the different discharging plasma species and in the thermal energy, whether the Comsol software or the self-written fluid model is used.

Keywords: self-coagulation of mass and energy; physically and chemically ambi-polar type; Schrodinger equation; β^- decay; neutrino; asymmetry; spin orientation; photon model; inter-disciplinary work

I. Introduction

The self-coagulation was earliest found in anion Comet structure given by the fluid simulation of Ar/O_2 ICP source [1]. It was analyzed that this coagulated comet structure corresponds to the free diffusion component and negative chemical source of O^- anions. A quasi- Helmholtz equation constructed based on these two terms can be solved analytically and a delta function was found one of its testing solutions, which explains the coagulation of anions. In Ref. [2], based on the *precise* Helmholtz equation with *positive* source term that can be transformed to the *normal* spring oscillation model with *retrieving* force and the quasi- Helmholtz equation with negative source term that can be transformed to the revised spring oscillation model with dispersing force, the trigonometric and sine

 doi:10.20944/preprints202604.0734.v1

function solution for electropositive plasma and the delta function solution for electronegative plasma were built, respectively.

In Ref. [3], the exploration of self-coagulation was extended from the low-electronegative Ar/O_2 ICP to the high-electronegative Ar/SF_6 ICP. First, when the pressure is low, 20mTorr, besides for the self-coagulation, one type of early discovered classical electronegative discharge structure, stratification into core and halo [4] and related parabola profile of core[5], was still found. It is known that the preceding and classical core parabola theory was achieved at utilizing the assumption of electrons and anions Boltzmann balances. In our fluid simulation of Ar/SF_6 ICP, the anion Boltzmann balance is calculated self-consistently and its driving force is related to the self-coagulation. Besides, at the interface of electronegative core and electropositive halo, rich microscopic wave dynamic structure, i.e., double layer[6], is formed, which is essentially an acoustic wave intrinsically imposed by the Landau damping[7], as the detail analysis revealed. All these discharge characteristics at the high-electronegativity and low-pressure condition, are classified into three levels, i.e., macroscopic level of stratification, mesoscopic level of self-coagulation, and microscopic wave dynamics. And all these discharge levels constitute a complex discharge structure hierarchy of electronegative plasma.

Still in Ar/SF_6 ICP, when increasing the pressure to 90mTorr, the stratification described above disappears but the self-coagulation still exists, but with the density peak coagulated shifted from the parabola edge at the low pressure toward the coil, i.e., under the dielectric window, at the high pressure. Besides for the self-coagulation under the coil, all the peripherical region was covered by the flattened and ellipse profile, which is another early discovered classical electronegative discharge structure[8]. It is mentioned that when increasing the Ar/SF_6 ICP pressure from 20 mTorr to 90 mTorr, the discharge structure hierarchy consisted of stratification, parabola core, self-coagulation and double layer that is formed in the regime of transport dominated, turns into the hierarchy consisted of self-coagulation, ellipse, blue sheath and ionization instability that is formed in the regime of chemistry dominated[9].

In Ref. [10], the Coulomb scattering between the quasi-particle with the same polarity given by the self-coagulation, i.e., among either the coagulated cations or the coagulated anions, was specially reported. In Ref. [11], the self-coagulation and related discharge structure in the Ar/Cl_2 ICP with the mediate electronegativity, and their evolutions with the discharge condition, were focused on. In this reference, the concepts of species-stratification and space-stratification was distinguished, and the mixed structures of self-coagulation and ellipse in this mediately electronegative Ar/Cl_2 ICP (without potential collapse) and the highly electronegative Ar/SF_6 ICP (with potential collapse) were compared. Still there, the novel hollow discharge type and related self-grouping effect were firstly reported and the replacement of this defined chemical self-coagulation by the physical coagulation with the variation of discharge condition was also covered. In Refs. [9,12], the different discharge structure hierarchies revealed in the field of low temperature plasma were correlated to the fields of astrophysics (formations of artificial star and planet using self-coagulation instead of gravitation), particle physics (coagulation and ellipse, and the blue sheath, represent the neutron, proton, and meson, respectively), geophysics (earth structure morphologically corresponds the discharge structure hierarch of low-pressure Ar/SF_6 ICP), quantum physics (mixed structure of ellipse and coagulation corresponds the wave-particle duality), and nuclear fusion (an idea of free and self-fusion replacing the constrained fusion), aimed at the help people acquire the objective essential of the abstracted physical models.

As the electronegative plasma studies revealed, self-coagulation is always accompanied by the complex discharge structure and the self-coagulation holds different features in different discharge hierarchies given by the different electronegativities and pressures. Moreover, if the condition is suitable, it is discovered that the metastables in the electropositive argon ICP sourced can self-coagulate as well. All the self-coagulation discovered presently are classified into the physically ambi-polar type, chemically ambi-polar type, mono-polar type and the non-polar type. All the above types are summarized as the self-coagulation of mass. Furthermore, in another electropositive argon ICP source that excludes the metastables but considers an elaborate electron collision energy

 doi:10.20944/preprints202604.0734.v1

consumption scheme, the self-coagulation of energy is still discovered. In the present article, all these types of mass and energy self-coagulations are reported and their implications on the activity of ambi-polar diffusion, particle physics (positive and reverse particle pair), quantum physics (duality and applicability of Schrodinger equation), nuclear physics (β decay), the spins of neutrino and anti-neutrino, and the photon model, are revealed as well. All these efforts aim at helping human understand better the mass world they live in, with a deep inter-disciplinary network.

The outline of article is as follows. In Section II. the methodology is given, where (1) the fluid simulations of four types of ICP source (Ar/SF_6, Ar/O_2, Ar/Cl_2, and pure argon) with Comsol software served for the self-coagulation of mass, (2) the fluid simulation of a special argon ICP source with self-written code served for the self-coagulation of energy, and (3) the three analytical theories, i.e., the parabola core (suitable for the low pressure Ar/SF_6 ICP), the ellipse background (suitable for the high pressure Ar/SF_6 ICP and the metastable of Ar ICP with Comsol), and the self-coagulation (suitable for the mass and energy), are sequentially described. In Section III, the results are discussed and in Section IV, a conclusion is given.

II. Methodology

2.1. Fluid Simulations of ICP Sources with Comsol Software

In this study, the fluid model is used to simulate the Ar/SF_6, Ar/O_2, and Ar/Cl_2 mixed ICP sources and a pure argon ICP source. The behind physics and chemistry of these simulations are partially explained based on the discharge structure theories given in the next Section 2.3. The equations of electron density and energy density of fluid model are given as follows.

$$\frac{\partial n_e}{\partial t}+\nabla\cdot\mathbf{\Gamma}_e=R_e, \tag{1}$$

$$\frac{\partial n_\varepsilon}{\partial t}+\nabla\cdot\mathbf{\Gamma}_\varepsilon+\mathbf{E}\cdot\mathbf{\Gamma}_e=R_\varepsilon+P_{ohm}. \tag{2}$$

Herein, n_e and n_ε are the number density and energy density of electrons, respectively. $\mathbf{\Gamma}_e$ and $\mathbf{\Gamma}_\varepsilon$ are the corresponding fluxes of number density and energy density of electrons, respectively. R_e and R_ε are the corresponding source terms for the number density and energy density of electrons, respectively. P_{ohm} is the deposited power density via the electron Ohm heating scheme of RF field in the azimuthal direction, i.e., $P_{ohm}=\frac{1}{2}\mathrm{Re}\left(\sigma_e\left|E_\theta\right|^2\right)$, in which σ_e is the electrical conductivity of electrons and E_θ is the azimuthal RF field (see next). It is seen that the energy deposition process of ICP source in our selected fluid model is self-consistent. And, $\mathbf{E}$ is the electrostatic field vector in the radial and axial directions. For solving the electron equation, the reduced mobility of electrons, $\mu_e N_n=8.23\times10^{23}\ (\mathrm{V^{-1}\cdot m^{-1}\cdot s^{-1}})$ is used and the other transport coefficients of electrons reported in Ref. [10], electron diffusion coefficient and electron energy diffusion and mobility coefficients, are then calculated via this reduced mobility. It is noted that the expression of electron energy equation of COMSOL software is different and the electrons heat conduction cofficient is expressed by the electron energy diffusion and mobility coefficients.

The mass fraction equation is used to describe the mass transport of heavy species in Equation (3).

$$\rho\frac{\partial w_k}{\partial t}=\nabla\cdot\mathbf{j}_k+R_k. \tag{3}$$

 doi:10.20944/preprints202604.0734.v1

Herein, ρ is the total mass density of heavy species and w_k is the mass fraction of species k. $\mathbf{j}_k$ is the diffusive and drift flux of species k. It is noted the heavy species temperature is assumed to be room temperature, which satisfies the quasi- cold ions approximation as mentioned in Section I. The diffusion coefficients of heavy species in Equation (3) are calculated through the Chapman-Enskog method based on the Lennard-Johns potential with the potential characteristic length and potential energy minimum parameters, i.e., σ and ε. The mobilities of heavy species are then calculated by the diffusion coefficients through the Einstein's relation.

To describe the azimuthal RF field in the reactor, the Maxwell equations are combined to express the Ampere law in Equation (4).

$$(j\omega\sigma_e - \omega^2\varepsilon_0\varepsilon_r)\mathbf{A} + \nabla\times(\mu_0^{-1}\mu_r^{-1}\nabla\times\mathbf{A}) = \mathbf{J}_a. \tag{4}$$

Herein, j is the imaginary unit and ω is the angular frequency of power source, expressed as $2\pi f$ at $f = 13.56\text{MHz}$. ε_0 and ε_r are the vacuum permittivity and the relative permittivity of dielectric window material (quartz), respectively. μ_0 and μ_r are the vacuum permeability and the relative permeability of coil that is made of copper, respectively. $\mathbf{A}$ is the magnetic vector potential, from which the RF magnetic and electric fields are calculated as, $\mathbf{B} = \nabla\times\mathbf{A}, \mathbf{E}_{rf} = -\dfrac{\partial\mathbf{A}}{\partial t}$. When considering the azimuthal symmetry, only the azimuthal component of RF electric field, E_θ, and the axial and radial components of RF magnetic field, B_r, B_z, need to be addressed. $\mathbf{J}_a$ is the applied coil current density and its magnitude is varied until the required power, 300 W, is achieved. σ_e is the electron conductivity[10] and expressed as, $\sigma_e = \dfrac{n_e q^2}{m_e(\nu_e + j\omega)}$.

The Poisson equation is used to calculate the electrostatic field in Equation (5).

$$\begin{aligned} \mathbf{E} &= -\nabla V, \\ \nabla\cdot\mathbf{D} &= \rho_V. \end{aligned} \tag{5}$$

Herein, $\mathbf{D}$ is the electric displacement vector, from which the electrostatic field can be deduced through the permittivity, and ρ_V is the spatial charge density. Most of the boundary conditions used for the above equation is given in Ref. [10], and herein only the heavy species wall boundary conditions are described, i.e., $\Gamma_- = 0$, $\Gamma_+ = \left(\dfrac{\gamma_f}{1-\gamma_f/2}\right)\dfrac{1}{4}n_+\sqrt{\dfrac{8RT}{\pi M_W}} + \mu_+ n_+ E$, $\Gamma_n = \Gamma_+$, $\Gamma_{F_2} = \dfrac{1}{2}\Gamma_F$. Herein, γ_f is the sticking coefficient.

The Ar/SF_6 gas-phase chemistry includes the elastic collision, the excitation and deexcitation, the ionization, the direct and dissociative attachments, and the dissociation of the electron-impact. The heavy species reactions include the neutral and ionic recombination, the detachment, the Penning ionization and the charge exchange. The surface kinetics of species include the recombination and the de-excitation. The ICP reactor consists of the vacuum chamber, the dielectric window and the plasma chamber. The radius of dielectric window and vacuum chamber is 14 cm, and the heights of them are 1 cm and 3 cm, respectively. The radius of plasma chamber is 15 cm and the height of it is 13 cm. To simulate the plasma processing technique, the substrate with a radius of 13 cm and a height of 4 cm is seated at the bottom center of plasma chamber. The two-turn coil is installed above the dielectric window and the radial locations of two turns are 8 cm and 10 cm, respectively. More detail about the fluid model of Ar/SF_6 ICP source, such as the reaction list and surface kinetics and ICP configuration, can be found in Ref. [10]. As stated in Ref. [10], electron-impact cross sections from the

 doi:10.20944/preprints202604.0734.v1

lxcat website database based on the Maxwellian electron energy distribution function and the Arrhenius chemical rates are used together, for constructing the Ar/SF_6 chemistry. Since there are many types of cations and anions in the Ar/SF_6 chemistry, such as SF_6^-, SF_5^-, SF_4^-, SF_3^-, SF_2^-, F^-, F_2^-, and SF_5^+, SF_4^+, SF_3^+, SF_2^+, SF^+, F^+, F_2^+, S^+, Ar^+, the summed cations and anions densities are presented. For the net source of anions, all the attachments that give any species of the above anions (positive), all the detachments that deletes any species of the above anions (negative), and all recombinations of cations and anions that delete any species of the above anions (negative), are summed. It is noted that the negative source of anions in the self-coagulation dynamics is dominated by the recombination of cations and anions, rather than the detachments of anions, which is different with the electronegative CCPs that operate at relatively high pressures.

As mentioned before, in the Comsol software, besides for the Ar/SF_6 ICP source, the Ar/O_2 ICP, Ar/Cl_2 ICP, and pure argon ICP sources are simulated as well by the fluid model. The inertia argon gas discharging ICP source uses the same Ar gas phase and surface chemistry as the mixed Ar/SF_6 ICP. For the Ar/O_2 and Ar/Cl_2 ICPs, the similar gas phase and surface chemistry as the Ar/SF_6 plasma is used. For the Ar/O_2 ICP chemistry, the anion type considered is O^- and the cation types considered are Ar^+, O^+, and O_2^+. For the Ar/Cl_2 ICP chemistry, the anion type considered is Cl^- and the cation types considered are Ar^+, Cl^+ and Cl_2^+. In addition, for the above three electronegative Ar/SF_6, Ar/O_2 and Ar/Cl_2 ICP sources, the main creation source of anions is attachment and the main consumption source of anions is recombination, and the net source of anions is to deduct the attachment with recombination. The main creation source of cations is ionization and the main consumption of cations is recombination as well, and the net source of cations is to deduct the ionization with recombination. The main creation source of electrons is ionization and the main consumption of electrons is attachment, and the net source of electron is to deduct the ionization with attachment. For the pure argon ICP source, the metastable argon atoms chemical kinetics are studied. The main creation of metastable is excitation and the main consumption of metastable is multi-step and Panning ionizations, and the net source of metastable is to deduct the excitation of metastable with multi-step and Panning ionizations. More details of chemistry involving the above four ICP source utilized in the fluid simulation of Comsol software can be found in Refs. [1,10,11]. These four types of ICP source fluid simulations are used to analyze the mass self-coagulation dynamics. In the next section, a fluid simulation of ICP source with the self-written code is described and used to analyze the energy self-coagulation.

2.2. Fluid Simulation of Argon ICP Source with Self-Written Code

$$\frac{1}{r}\frac{\partial}{\partial r}\left(r\frac{\partial E_\theta}{\partial r}\right)+\frac{\partial^2 E_\theta}{\partial z^2}-\frac{E_\theta}{r^2}+\varepsilon_0\mu_0\omega^2 E_\theta = i\omega\mu_0 J_\theta, \tag{6}$$

$$J_\theta = \sigma_e E_\theta, \tag{7}$$

$$\frac{\partial n_e}{\partial t}+\nabla\cdot\mathbf{\Gamma}_e = R_e, \tag{8}$$

$$\mathbf{\Gamma}_e = -\frac{\nabla\left(n_e kT_e\right)}{m_e\nu_{en}}-\frac{en_e}{m_e\nu_{en}}\mathbf{E}, \tag{9}$$

$$R_e = k_i(T_e)n_e n_a, \tag{10}$$

$$\frac{\partial}{\partial t}\left(\frac{3}{2}n_e kT_e\right) = -\nabla\cdot\mathbf{q}_e - e\mathbf{\Gamma}_e\cdot\mathbf{E}-E_e+P_{ind}, \tag{11}$$

 doi:10.20944/preprints202604.0734.v1

$$\mathbf{q}_e = \frac{5}{2}\mathbf{\Gamma}_e kT_e - \frac{5}{2}\frac{n_e kT_e}{m_e \nu_{en}}\nabla\left(kT_e\right), \tag{12}$$

$$E_e = \sum \varepsilon_c k_i(T_e) n_e n_a, \tag{13}$$

$$P_{ind} = \frac{1}{2}\mathrm{Re}\left(\sigma_e \left|E_\theta\left(r,z\right)\right|^2\right), \tag{14}$$

$$\frac{\partial n_i}{\partial t} + \nabla \cdot n_i \mathbf{u}_i = R_i, \tag{15}$$

$$\frac{\partial n_i m_i \mathbf{u}_i}{\partial t} + \nabla \cdot \left(n_i m_i \mathbf{u}_i \mathbf{u}_i\right) = -kT_i \nabla n_i + e n_i \mathbf{E} - \mathbf{M}_i, \tag{16}$$

$$\nabla^2 \varphi\left(r,z\right) = -\frac{e}{\varepsilon_0}\left(n_i - n_e\right), \mathbf{E} = -\nabla\varphi, \tag{17}$$

$$\mathbf{\Gamma}_e = \frac{1}{4} n_e v_{th} \exp\left(\varphi_w / kT_e\right)\mathbf{n}, \mathbf{q}_e = 2\mathbf{\Gamma}_e kT_e. \tag{18}$$

In this section, the fluid simulation of argon ICP source that excludes the metastable but considers an elaborate electron energy scheme is introduced. In Equation (6), the Helmholtz equation that considers the azimuthal plasma current is used to calculate the azimuthal electric field. In Equation (7), the azimuthal plasma current is correlated to the electron conductivity that is expressed in Equation (4), which represents the Ohm law. In Equations (8)-(10), the electron continuity equation, flux and source term are expressed. In Equations (11)-(14), the electron energy density equation, energy flux, collision energy consumption, and deposited inductive type of power are expressed. In Equations (15) and (16), the ion continuity and momentum equations are expressed. In Equation (17), the Poisson equation is given to calculate the electrostatic field and In Equation (18), the boundary conditions used for electron equations, Equations (8) and (11), are presented. The electron collision energy consumption is focused on the grounded ionization and excitations. The excitation scheme considered is elaborate, which includes five excitation states, $\mathrm{Ar}[4s'_{1/2}, 4s_{3/2}]$, $\mathrm{Ar}[3d'_{3/2}]$, $\mathrm{Ar}[3d_{3/2}]$, $\mathrm{Ar}[5s'_{1/2}]$, and $\mathrm{Ar}[5s_{3/2}]$. This detailed electron collision energy loss mechanism, together with the Ohm heating scheme of Equations (7) and (14), ensures a self-consistent analysis of energy self-coagulation in Section 3.5.

Herein, in Equations (6) and (7), j_θ and E_θ are the azimuthal plasma current and electric field, respectively. In Equation (8), n_e, $\mathbf{\Gamma}_e$ and R_e are the electron density, the electron flux, and the chemical source (grounded ionization), respectively. In Equation (9), k and T_e are the Boltzmann constant and the electron temperature, respectively. m_e, ν_{en}, and $\mathbf{E}$ are the electron mass, the electron elastic collision frequency, and the electrostatic field, respectively. In Equation (10), k_i and n_a are the grounded ionization rate coefficient and the target argon density, respectively. In Equation (11), $\mathbf{q}_e$, E_e, and P_{ind} are the electron energy flux, the electron inelastic collision energy loss (including ionization and excitations), and the deposited inductive type of power, respectively. In Equation (12), the electron energy flux considers the contributions of advection and thermal conductivity. In Equation (13), ε_c is the electron inelastic collision threshold. In Equation (14), the

 doi:10.20944/preprints202604.0734.v1

Ohm heating mechanism is taken. In Equation (15), n_i, $\mathbf{u}_i$ and R_i are the argon ion Ar^+ density, the Ar^+ species fluid velocity, and the Ar^+ species chemical source (grounded ionization), respectively. In Equation (16), the full momentum ion equation is considered, which includes the inertia term, advection term, pressure gradient, drift, and ion dragging force because of ion and neutral collision. T_i and $\mathbf{M}_i$ are the ions temperature (300 K) and the collision transfer of momentum from ions to neutrals, respectively. In Equation (17), φ is the electric potential. In Equation (18), v_{th} and φ_w are the electron thermal velocity and the potential at the wall, respectively. Lastly, $\mathbf{n}$ is the unit normal vector oriented to the wall. More details of the self-written fluid model of argon ICP source can be found in Refs. [13–15].

2.3. Analytical Theories Related

(a) Parabola theory

In the parabola theory, the ambi-polar diffusion process is adopted. It is arisen from the electropositive plasma that consists of electron and ion. The electronegative plasma is made of cation, anion and electron and it is a triple-species system. Here, the ambi-polar diffusion process of cation, anion and electron is constructed for the transport of electronegative plasma.

Whatever the transport scheme is, in the bulk plasma, the electrical neutrality is required. So, the flux equilibrium and charge density equilibrium exist in the electronegative plasma. In the Equations (19, 20), the flux and density balances between the cation, anion and electron are expressed. Herein, Γ_+, Γ_- and Γ_e are the fluxes of cation, anion and electron, respectively. n_+, n_- and n_e are the densities of cation, anion and electron, respectively. The electronegativity α is given in Equation (21), defined as the ratio of anion density over the electron density. Next, the fluxes of cation, anion and electron calculated at the drift and diffusion approximation of momentum balance equation are given in Equations (22)-(24). Herein, D_+, D_- and D_e are the diffusion coefficients of cation, anion and electron, respectively. μ_+, μ_- and μ_e are the mobilities of cation, anion and electron, respectively. The electric field E in the drift term is electrostatic and determined by the ambi-polar diffusion potential gradient of electronegative plasma. These previous six equations, i.e., Equations (19)-(24), are correlated and the flux of cation is accordingly rewritten as a function of the quantities, μ_+, μ_-, μ_e, D_+, D_-, D_e, n_+, n_-, n_e and α, illustrated in Equation (25). Like the electropositive plasma, the ambi-polar diffusion coefficient of electronegative plasma, D_{a+}, is introduced. The cation flux is thus re-expressed as a product of this newly introduced coefficient and the cation density gradient, illustrated in Equation (26).

$$\Gamma_+ = \Gamma_- + \Gamma_e, \tag{19}$$

$$n_+ = n_- + n_e, \tag{20}$$

$$\alpha = n_- / n_e, \tag{21}$$

$$\Gamma_+ = -D_+ \nabla n_+ + n_+ \mu_+ E, \tag{22}$$

$$\Gamma_- = -D_- \nabla n_- - n_- \mu_- E, \tag{23}$$

 doi:10.20944/preprints202604.0734.v1

$$\Gamma_e = -D_e \nabla n_e - n_e \mu_e E, \tag{24}$$

$$\Gamma_+ = -\frac{(\mu_e + \mu_- \alpha) D_+ + \mu_+ (1+\alpha) D_e (\nabla n_e / \nabla n_+) + \mu_+ (1+\alpha) D_- (\nabla n_- / \nabla n_+)}{\mu_e + \mu_- \alpha + \mu_+ (1+\alpha)} \nabla n_+, \tag{25}$$

$$\Gamma_+ = -D_{a+} \nabla n_+. \tag{26}$$

As seen above, the deduced ambi-polar diffusion coefficient of electronegative plasma in Equation (25) is quite complicated. So, reasonable approximations need to be introduced to reduce its complexity and more clear physics can thereby emerge. To arrive at this goal, the significant difference between the electron and anion temperatures is first noticed, which characterizes the non-thermal equilibrium plasma that is generated through the radio frequency glow discharge. The parameter, $\gamma = T_e / T_i$, is thus introduced, which is defined as the ratio of electron temperature over the anion temperature. Herein, T_e and T_i are the electron and anion temperatures, respectively. It is noticed that the anion and cation are in the thermal equilibrium and hence their temperatures are the same. Then, by utilizing the Boltzmann balances of both electron and anions, and the correlations between the diffusion coefficients and mobilities of different species based on the Einstein's formula, the complex D_{a+} is simplified in Equation (27).

$$D_{a+} = D_+ \frac{(1+\gamma+2\gamma\alpha)\left(1+\alpha\frac{\mu_-}{\mu_e}\right)}{(1+\gamma\alpha)\left(1+\frac{\mu_+}{\mu_e}(1+\alpha)+\frac{\mu_-}{\mu_e}\right)}. \tag{27}$$

After the present simplification, the ambi-polar diffusion coefficient is now a function of quantities, D_+, α, γ, and the mobilities, μ_+, μ_-, μ_e. At noticing the significant difference between the mobilities of the heavy cation and anion and the electron's mobility that is illustrated in Equation (28), the coefficient can be further simplified in Equation (28). Moreover, if the electronegativity α is rather high, which is just the assumed condition of the Ar/SF_6 ICP, it is again simplified to be a constant, $2D_+$, as illustrated in Equation (29). As seen next, the constant ambi-polar diffusion coefficient value, which is obtained after a set of simplifications, is very helpful for us to analyze the transport of electronegative plasma and the structure that it forms.

$$\mu_- / \mu_e, \mu_+ / \mu_e \ll 1, D_{a+} \cong D_+ \frac{1+\gamma+2\gamma\alpha}{1+\gamma\alpha}, \tag{28}$$

$$\alpha \gg 1, D_{a+} \cong 2D_+. \tag{29}$$

Still, at the Boltzmann balances of both the electron and anion, and further considering the large value of γ parameter, the electron density tends to constant, n_{e0}. In Equation (30), the continuity equation of cation is given. At the left side of equation, the flux is expressed as a product of the ambi-polar diffusion coefficient and the density gradient of cation. At the right side of equation, the chemical sources include the ionization reactions for the creation of cation and the recombination reactions for the depletion of cation. Herein, n_0 is the density of target neutral atom for the electron collisions. K_{iz} and K_{rec} are the rate coefficients of the ionization and recombination reactions, respectively. In Equation (31), the continuity equation is significantly simplified as follows. Firstly, at

 doi:10.20944/preprints202604.0734.v1

the left side of continuity equation, the ambi-polar diffusion coefficient that is originally a function of electronegativity is replaced by the constant value given above in Equation (29), $2D_+$. Then, at the right side of continuity equation and in the ionization reaction term, the electron density that is originally spatially varied is replaced by the constant value, n_{e0}. Still, the recombination loss term for the cation at the right side of equation is neglected, assuming the influence of recombination is insignificant that is validated by the low pressure fluid simulation of Ar/SF_6 ICP. The simplified continuity equation of cation in Equation (31) after the set of above operations can be analytically solved, which is a parabola function as shown in Equation (32). Herein, α_0 is the electronegativity of center and l is the nominal position where the electronegativity is zero and then the anions disappear, i.e., the interface of stratification. Herein, a brief introduction of parabola theory is given and more details of it can be found in Refs. [9,12].

$$-\frac{d}{dx}\left(D_{a+}(\alpha)\frac{dn_+}{dx}\right)=K_{iz}n_0n_e-K_{rec}n_+n_-, \tag{30}$$

$$-2D_+\frac{d^2n_+}{dx^2}=K_{iz}n_0n_{e0}, \tag{31}$$

$$\frac{n_+}{n_{e0}}=\alpha_0\left(1-\frac{x^2}{l^2}\right)+1, \tag{32}$$

(b) Ellipse theory

$$\frac{d}{dx}\left(-D_+\frac{dn_+}{dx}+n_+\mu_+E\right)=K_{iz}n_0n_e-K_{rec}n_+n_-, \tag{33}$$

$$\frac{d}{dx}\left(-D_-\frac{dn_-}{dx}-n_-\mu_-E\right)=K_{att}n_0n_e-K_{rec}n_+n_-, \tag{34}$$

$$\frac{d}{dx}\left(-D_+\frac{d}{dx}n_+-\mu_+n_+\frac{D_e}{\mu_e}\frac{1}{n_e}\frac{dn_e}{dx}\right)=K_{iz}n_0n_e-K_{rec}n_+n_-, \tag{35}$$

$$\frac{d}{dx}\left(-D_+\frac{d}{dx}(n_+-n_e)+\mu_+(n_+-n_e)\frac{D_e}{\mu_e}\frac{1}{n_e}\frac{dn_e}{dx}\right)=K_{att}n_0n_e-K_{rec}n_+n_-, \tag{36}$$

$$\frac{d}{dx}\left(-2D_+\frac{dn_+}{dx}-\gamma D_+\frac{dn_e}{dx}\right)\approx(K_{iz}+K_{att})n_0n_e-2K_{rec}n_+n_-, \tag{37}$$

In Equations (33) and (34), the continuity equations of cations and anions are given. Herein, the approximated drift and diffusion fluxes are adopted for the ions. The Boltzmann balance is used for the electrons but not for the anions, which is different with the parabola theory. Using the electron Boltzmann balance, the Einstein formula, the relation between the electric field and potential gradient, $\vec{E}=-\nabla\varphi$, and the electrical neutrality, the continuity equations of cations and anions are reformed in Equations (35) and (36), neglecting the differences of the transport coefficients of cations and anions. Furthermore, the two continuity equations in Equations (35) and (36) are added and the Equation (37) is obtained. Observing the Equation (37), it is seen that the two terms at the left side of equation can be compared. As seen, if the term, $\gamma D_+\frac{dn_e}{dx}$, is negligible the reformed continuity

 doi:10.20944/preprints202604.0734.v1

equation can be solved analytically and it is found that the cations/anions density is in fact an elliptic profile. So, the inequality, i.e., $\left|\frac{\gamma d^2 n_e / dx^2}{2 d^2 n_+ / dx^2}\right| \ll 1$, becomes a criterion of the ellipse theory, which is also validated by the Ar/SF_6 ICP fluid simulation at high pressure since the electron density profile is indeed smoother than the ions.

$$\beta(\alpha) = -2D_+ n_{e0} \frac{d\alpha}{dx}, \tag{38}$$

$$-\frac{1}{4D_+ n_{e0}} \frac{d}{d\alpha}\beta^2 = \left(K_{iz} + K_{att}\right) n_0 n_{e0} - 2K_{rec} n_{e0}^2 \alpha(\alpha+1), \tag{39}$$

$$\beta(\alpha) = \beta_0 \left[(\alpha_0 - \alpha) - \frac{2K_{rec} n_{e0}}{\left(K_{iz} + K_{att}\right) n_0} \times \left(\frac{\alpha_0^3 - \alpha^3}{3} + \frac{\alpha_0^2 - \alpha^2}{2} \right) \right]^{1/2}, \tag{40}$$

$$\beta_0 = \left[4D_+ \left(K_{iz} + K_{att}\right) n_0 n_{e0}^2 \right]^{1/2}, \tag{41}$$

$$\int_{\beta(\alpha_0)}^{\beta} d\beta^2 = \int_0^{\beta} d\beta^2 = \beta^2, \beta(\alpha_0) = 0, \frac{d\alpha}{dx}\Big|_{x=0\,(\alpha=\alpha_0)} = 0. \tag{42}$$

Next, we deduce the ellipse theory of electronegative plasma at the above inequality. The implications of the inequality condition are illustrated as follows, $\gamma D_+ \frac{dn_e}{dx} \approx 0, n_e \sim n_{e0}$ and $n_+ = n_{e0}(\alpha+1), n_- = n_{e0}\alpha, n_+ n_- = n_{e0}^2 \alpha(\alpha+1)$. In Equation (38), a new variable, β, as a function of $\frac{d\alpha}{dx}$ is introduced. Then, the continuity equation in Equation (37) is further reformed to be the Equation (39). It is seen that the newly reformed continuity equation is a first-order differential equation and its independent variable is the electronegativity α now, instead of x. By integrating this differential equation, a new expression is obtained for β in Equation (40), at the assistance of a parameter β_0 defined in Equation (41). It is noticed that during this integral process, the cylindrical symmetry condition at the center, which represents the lower integral limit, is used, as shown in Equation (42).

$$x(\alpha) = \int_{\alpha(x)}^{\alpha_0} \frac{2D_+ n_{e0}}{\beta(\alpha)} d\alpha, \tag{43}$$

$$x(\alpha) = \frac{2D_+ n_{e0}}{\beta_0} \int_{\alpha(x)}^{\alpha_0} \frac{d\alpha}{\left[(\alpha_0 - \alpha) - \frac{2K_{rec} n_{e0}}{\left(K_{iz} + K_{att}\right) n_0} \times \left(\frac{\alpha_0^3 - \alpha^3}{3} + \frac{\alpha_0^2 - \alpha^2}{2} \right) \right]^{1/2}}, \tag{44}$$

$$x(\alpha) = \frac{2D_+ n_{e0}}{\beta_0} \cdot \frac{\alpha_0}{(\eta/3)^{1/2}} \int_{\alpha(x)}^{\alpha_0} \frac{d\alpha}{(\alpha_0 - \alpha)^{1/2} \left\{ (-1) \times \left[\alpha^2 + \left(\alpha_0 + \frac{3}{2} \right) \alpha - \left(\frac{3\alpha_0^2}{\eta} - \alpha_0^2 - \frac{3}{2}\alpha_0 \right) \right] \right\}^{1/2}}, \tag{45}$$

 doi:10.20944/preprints202604.0734.v1

$$\eta = \frac{2K_{rec}n_{e0}\alpha_0^2}{(K_{iz}+K_{att})n_0}, \tag{46}$$

$$x = \frac{2D_+ n_{e0}}{\beta_0}\frac{\alpha_0}{(\eta/3)^{1/2}} \times \int_{\alpha(x)}^{\alpha_0} \frac{d\alpha}{\left[(b\alpha_0-\alpha)(\alpha_0-\alpha)(a\alpha_0+\alpha)\right]^{1/2}}, \tag{47}$$

$$\begin{cases} a = \frac{1}{2}+\frac{1}{2}\left(\frac{12}{\eta}-3\right)^{1/2}, \\ b = -\frac{1}{2}+\frac{1}{2}\left(\frac{12}{\eta}-3\right)^{1/2}. \end{cases} \tag{48}$$

Slightly reforming the initial expression of β in Equation (38) and then integrating it, the Equation (43) is obtained. At the left side of Equation (43), the spatial coordinate has been expressed as a function of the electronegativity, i.e., $x(\alpha)$. At the right side of it, the quantity, β, in the denominator of integrated term is substituted by its new expression in Equation (40) and then the Equation (44) is obtained. After this substitution, it is seen that the denominator is now a third-order polynomial of electronegativity, α. We now factorize the polynomial. At the first factorization, the Equation (44) is reformed to be the Equation (45) and the denominator becomes now a second-order polynomial of α, except for the factor, $\alpha_0-\alpha$. It is noticed that in the transformation of Equation (44) onto Equation (45), a new parameter, η, is introduced. It is a function of rates of recombination, ionization and attachment, as expressed in Equation (46). This is a very important parameter since it reveals the chemistry of Ar/SF_6 plasma and as reported in Ref. [12], when this parameter tends to one (i.e., chemistry dominance) the elliptic profile of ions is flattened. A second factorization leads to the Equation (47), with the new parameters, a, b, expressed in Equation (48). In a view of mathematics, the integral of Equation (47), $\int_{\alpha(x)}^{\alpha_0} \frac{d\alpha}{\left[(b\alpha_0-\alpha)(\alpha_0-\alpha)(a\alpha_0+\alpha)\right]^{1/2}}$, is an elliptical integral.

(c) Self-coagulation theory

The simulations show the self-coagulation always happens to the anions at first and there are both the ambi-polar self-coagulation and the mono-polar one. The self-coagulation related theories of anions have been described in Refs. [1,9,10,12], and herein the brief introduction of them is given. It is noted that not only anions (mass), but also electron mean energy self-coagulates. The steady-state continuity equation of anions that consists of the free diffusion flux and the negative source term given by the recombinations is expressed in Equation (49).

$$-D_-\nabla^2 n_- = -n_- n_+ k_{rec} = -n_-\nu_{rec}. \tag{49}$$

Introducing the parameter, $k_- = \sqrt{\frac{\nu_{rec.}}{D_-}}$, into Equation (49), the quasi-Helmholtz equation is obtained, as shown in Equation (50).

$$\nabla^2 n_- - n_-\frac{\nu_{rec.}}{D_-} = \nabla^2 n_- - n_- k_-^2 = \nabla^2 n - nk^2 = 0. \tag{50}$$

 doi:10.20944/preprints202604.0734.v1

For simplicity, the quantity subscripts are all removed in Equation (50). In Equation (51), this quasi-Helmholtz equation is reformed by the method of variable separation in the cylindrical coordinate system at the azimuthal symmetry assumption.

$$\begin{aligned} &\frac{1}{\rho}\frac{\partial}{\partial\rho}\left(\rho\frac{\partial n}{\partial\rho}\right)+\frac{\partial^2 n}{\partial z^2}-k^2 n=0,\\ &n(\rho,z)=R(\rho)Z(z),\\ &Z''+\nu^2 Z=0,\\ &\frac{d^2R}{d\rho^2}+\frac{1}{\rho}\frac{dR}{d\rho}-\left(k^2+\nu^2\right)R=0. \end{aligned} \tag{51}$$

Herein, ν^2 represents the eigenvalues. Utilizing the homogeneous boundary conditions of the above axial equation, the eigenvalues, ν^2, and the related eigenfunctions, $Z_m(z)$, are acquired in Equation (52).

$$\begin{aligned} &{\nu_m}^2=m^2\pi^2/l^2,\\ &Z_m=\sin(m\pi z/l),\\ &Z=\sum_{m=0}^{\infty}c_m Z_m=\sum_{m=0}^{\infty}c_m\sin(m\pi z/l). \end{aligned} \tag{52}$$

As seen, the above radial equation of Equation (51) is zero-order *imaginary* Bessel equation because of the negative source. Since the density value is limited at the center, the imaginary Bessel function, rather than the Hankel function, is selected. The expression for $R(r)$ is then obtained in Equation (53).

$$R=d_m I_0(\sqrt{k^2+{\nu_m}^2}\rho)=d_m I_0(\sqrt{k^2+m^2\pi^2/l^2}\rho). \tag{53}$$

The expression for $n(\rho,z)$, which is a product of $R(\rho)$ and $Z_m(z)$ is given in Equation (54).

$$\begin{aligned} n(\rho,z)=R(\rho)Z(z)&=\sum_{m=0}^{\infty}c_m\sin(m\pi z/l)\cdot d_m I_0(\sqrt{k^2+{\nu_m}^2}\rho)\\ &=\sum_{m=0}^{\infty}a_m\sin(m\pi z/l)\cdot I_0(\sqrt{k^2+m^2\pi^2/l^2}\rho). \end{aligned} \tag{54}$$

It is seen from Equation (55) the delta distribution unrelated to the spatial coordinates evolves at using the mathematic limit ideas to the obtained density, which indicates the physics of self-coagulation.

 doi:10.20944/preprints202604.0734.v1

$$n(\rho,z)=R(\rho)Z(z)=\sum_{m=0}^{\infty}a_m\sin(m\pi z/l)\cdot I_0(\sqrt{k^2+m^2\pi^2/l^2}\,\rho)$$
$$=\lim_{m\to\infty}\left[a_m\sin(m\pi z/l)\cdot\infty\right]=\lim_{m\to\infty}\left[a_m\sin(m\pi z/l)\cdot\lim_{z\to0}\frac{1}{z}\right]$$
$$=\lim_{z\to0}\left[\lim_{m\to\infty}a_m\sin(m\pi z/l)\cdot\frac{1}{z}\right]=\lim_{z\to0}\left[\lim_{m\to\infty}a_m\cdot\frac{\sin(m\pi z/l)}{z\pi/l}\cdot\frac{\pi}{l}\right] \quad (55)$$
$$=\lim_{\zeta\to0}\left[\lim_{m\to\infty}a_m'\cdot\frac{1}{\pi}\frac{\sin(m\zeta)}{\zeta}\right]=\lim_{\zeta\to0}\left[a_\infty'\lim_{m\to\infty}\frac{1}{\pi}\frac{\sin(m\zeta)}{\zeta}\right]$$
$$=a_\infty'\lim_{\zeta\to0}\delta(\zeta).$$

III. Results and Discussion

3.1. Physically Ambi-Polar Self-Coagulation of Ions at Low, Mediate and High Electronegativities of Plasma and Its Implication on Ambi-Polar Diffusion

In this section, the self-coagulation of anions at the low, mediate and high electronegativities are presented. The low electronegativity case is focused on the Ar/O_2 ICP, at the discharge conditions of 300W, 30mTorr and 10% of O_2 content. As the simulation revealed, at these conditions, the calculated electronegativity is about 0.15, as illustrated in Figure 1(c,a). The mediate electronegativity case is focused on the Ar/Cl_2 ICP, at the discharge conditions of 300W, 10mTorr and 5% of Cl_2 content. As the simulation revealed, at these conditions, the calculated electronegativity is about 2.1, as illustrated in Figure 3(c,a), The high electronegativity case is focused on the Ar/SF_6 ICP, at the discharge conditions of 300W, 10mTorr and 10% of SF_6 content. As the simulation revealed, at these conditions, the calculated electronegativity is about 46.6, as illustrated in Figures 5(a) and 6(c).

In Figure 1, the electron density, summed cations density, O^- density and plasma potential of Ar/O_2 ICP are presented. It is found the O^- density in Figure 1(c) exhibits a comet structure and the combination of this comet anion density and the smooth electron density profile (Figure 1(a)) constitutes a special summed cations density profile in Figure 1(b), for sustaining the electrical neutrality. Compare the Figure 1(c,d), the coagulated comet type of O^- is at the top of potential barrier, which implies the free diffusion transport component. In Figure 2, the O^- density, summed reaction rate of it, reaction rate of its generation, and reaction rate of its loss are presented. It is seen from Figure 2(a,b) at the position of O^- coagulation, the net source of it is negative. So, the free diffusion and negative chemical source are prepared, which explains well the coagulated comet type of O^- through the self-coagulation theory described in Section 2.3c. The similar story happens to the Ar/Cl_2 ICP shown in Figures 3 and 4. And the tiny difference is that Ar/Cl_2 ICP electronegativity is higher than the Ar/O_2 ICP, and so the combined cation density profile of Ar/Cl_2 ICP in Figure 3(b) is characterized by the comet structure, while the combined cation density profile of Ar/O_2 ICP in Figure 1(b) is characterized by smooth structure.

In Figure 5, the summed anions density, net source of anions and the plasma potential of Ar/SF_6 ICP at the low pressure of 10mTorr are presented. As reported in Ref. [16], at low pressure when the transport is dominated, the discharge of Ar/SF_6 ICP is stratified and the inner electronegative core and the outer electropositive halo are formed. It is seen from Figure 5, in the inner core, the anions density in Figure 5(a) is high, the net source of anions in Figure 5(b) is negative, and the potential distribution in Figure 5(c) is flat, which ensures the free diffusion of anions. Again, since these two conditions are satisfied the anion self-coagulation is happened, which explains the peak of anion density occurring in Figure 5(a) according to the theory of Section 2.3c. In Figure 6(a,b), the summed cations density and the net source of them in the Ar/SF_6 ICP source are given, and in Figure 6(c,d),

 doi:10.20944/preprints202604.0734.v1

the electrons density and the net source of them in the plasma source are given. It is seen that both the cations and electron hold the positive net source terms, especially for the cations. However, even with the positive source, the cations density of core in Figure 6(a) holds the same profile as anions in Figure 5(a), which implies the physically ambi-polar coagulation to ensure the electrical neutrality at the high electronegativity. This physical type of ambi-polar coagulation suits for the Ar/O_2 and Ar/Cl_2 ICPs as well since the chemical source of summed cations in the two sources are both positive as well (not shown here). This type of ambi-polar self-coagulation is like the ambi-polar diffusion that keep the plasma neutrality through the electrical interaction, and thereby it is defined as physically ambi-polar self-coagulation. However, this ambi-polar self-coagulation potential is weak since the masses of anions and cations are close, which thereby is in the order of ion temperature as shown in Ref. [17]. This is different with the ambi-polar diffusion potential of electron-ion pare plasma that is in the order of electron temperature. Besides, as the analytic theory in Section 2.3a predicted, except for the self-coagulation, the profile of ions in the core is parabolic. And when increasing the pressure, this parabola profile evolves into an ellipse (see the theory of Section 2.3b) and meanwhile the stratification disappears, as shown in the next section.

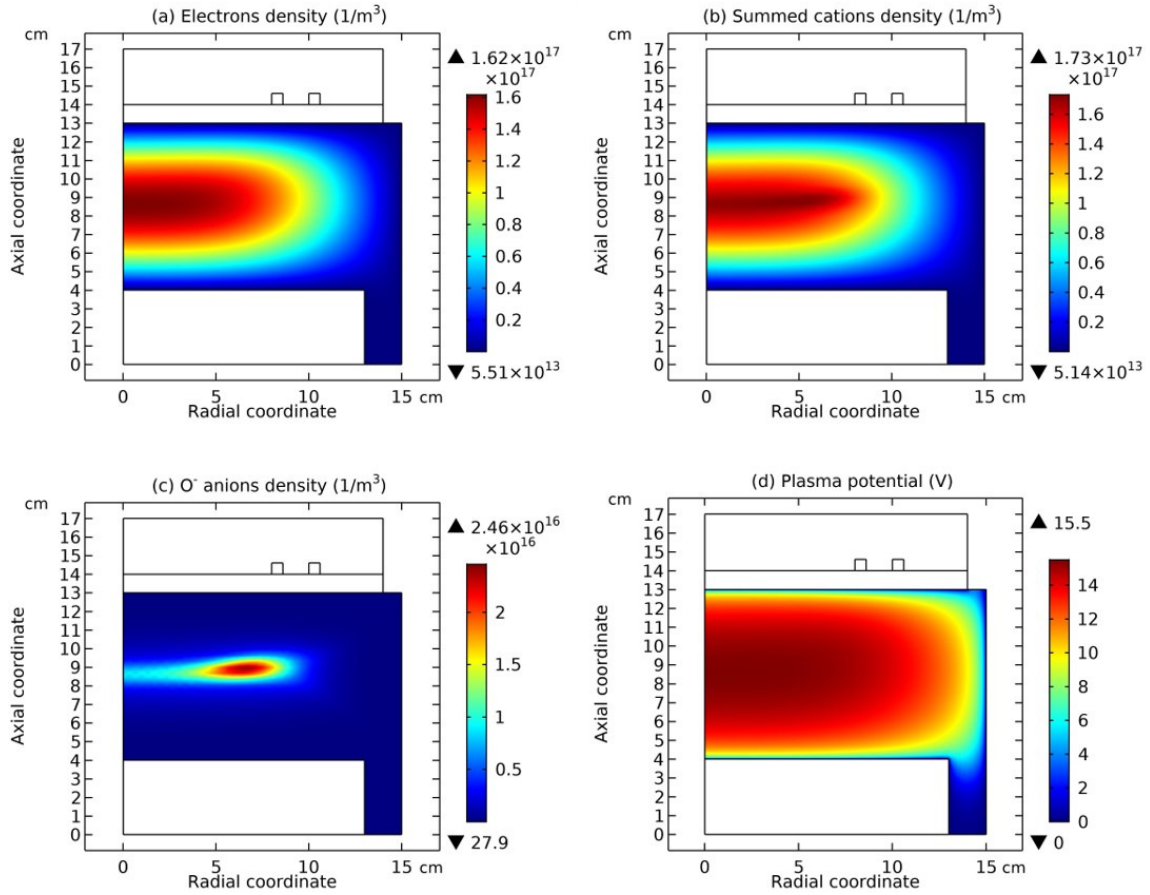

Figure 1. Electrons density (a), summed cations density (b), O^- anions density (c), and plasma potential (d) of Ar/O_2 ICP source, given by the fluid simulation at the discharge conditions of 300 W, 30 mTorr, and 10% reactive O_2 content in the gas mixture. The electronegativity of this plasma source is in an order of 0.1. The cations type can be found in Section 2.1.

Preprints.org (www.preprints.org) | NOT PEER-REVIEWED | Posted: 10 April 2026 doi:10.20944/preprints202604.0734.v1

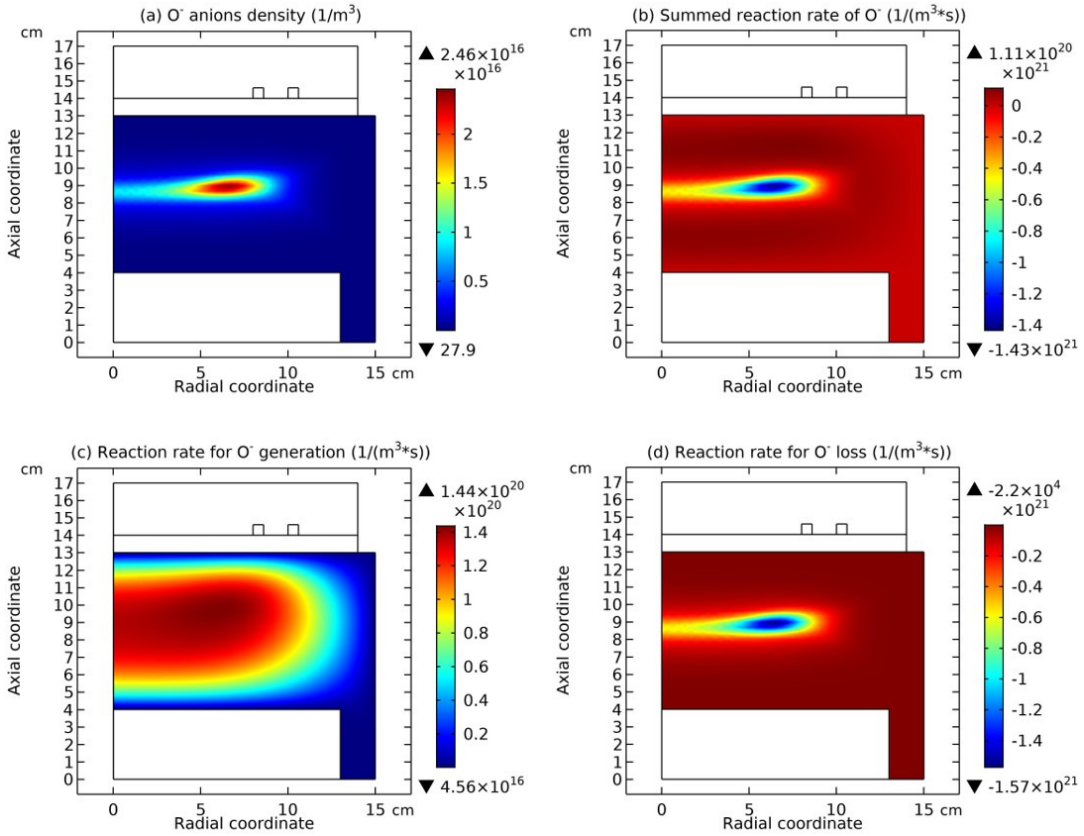

Figure 2. O^- anions density (a), summed reaction rate of O^- (b), reaction rate for O^- generation (c), and reaction rate for O^- loss (d) of Ar/O_2 ICP source, given by the fluid simulation. The discharge conditions and the electronegativity of this plasma source are the same as in Figure 1. The chemistry of O^- reaction can be found in Section 2.1.

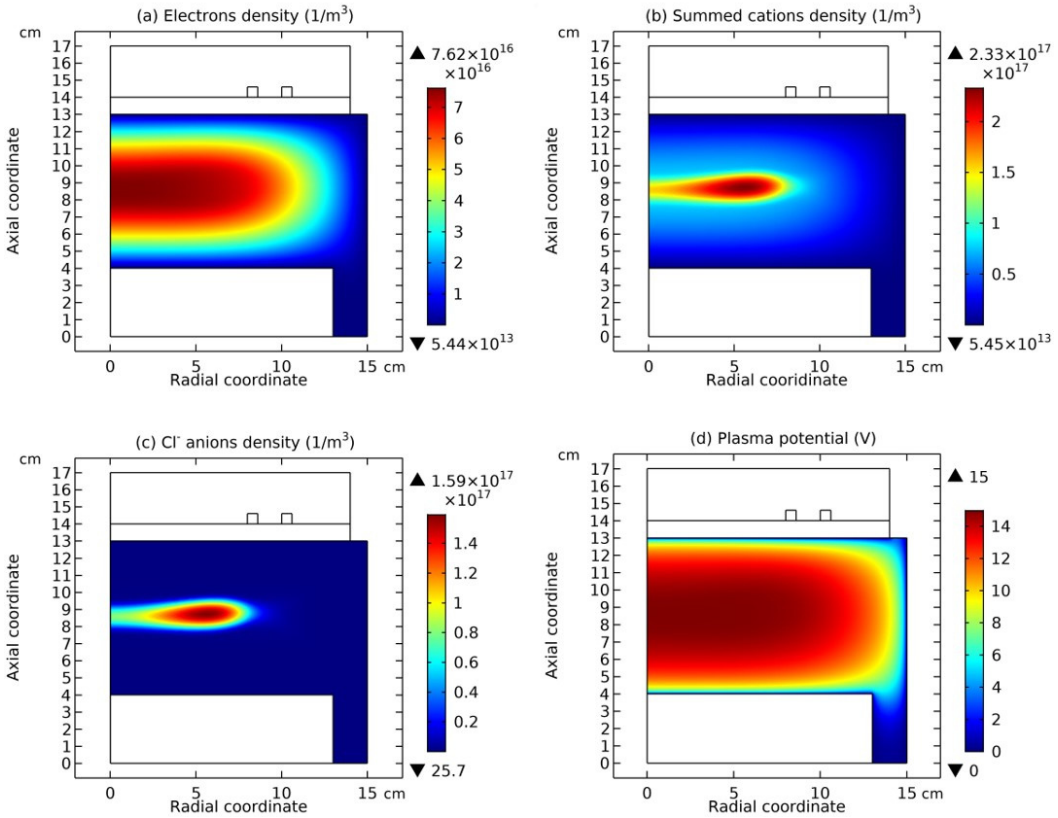

 doi:10.20944/preprints202604.0734.v1

Figure 3. Electrons density (a), summed cations density (b), Cl^- anions density (c), and plasma potential (d) of Ar/Cl_2 ICP source, given by the fluid simulation at the discharge conditions of 300 W, 10 mTorr, and five percent of reactive Cl_2 content in the gas mixture. The electronegativity of this plasma source is in an order of 10. The cations type can be found in Section 2.1.

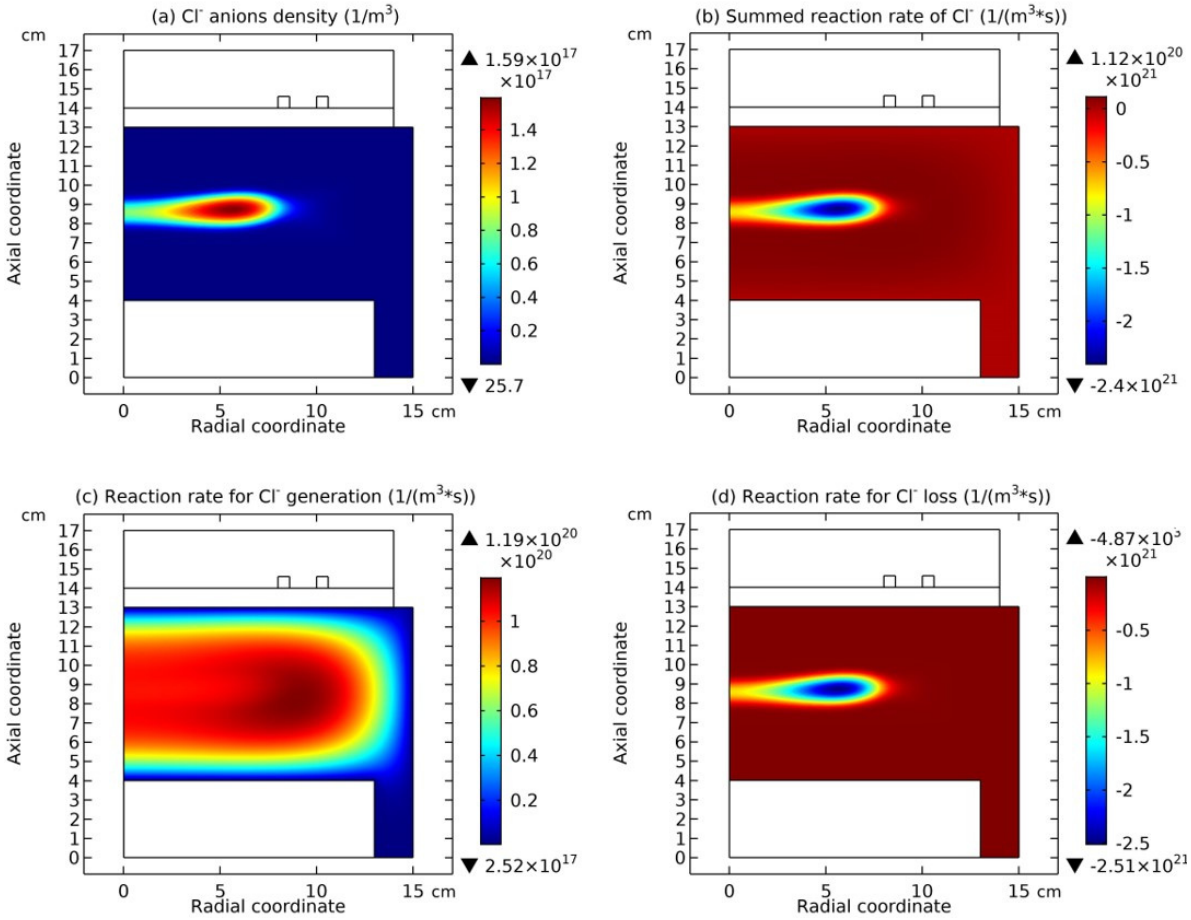

Figure 4. Cl^- anions density (a), summed reaction rate of O^- (b), reaction rate for Cl^- generation (c), and reaction rate for Cl^- loss (d) of Ar/Cl_2 ICP source, given by the fluid simulation. The discharge conditions and the electronegativity of this plasma source are the same as in Figure 3. The chemistry of Cl^- reaction can be found in Section 2.1.

 doi:10.20944/preprints202604.0734.v1

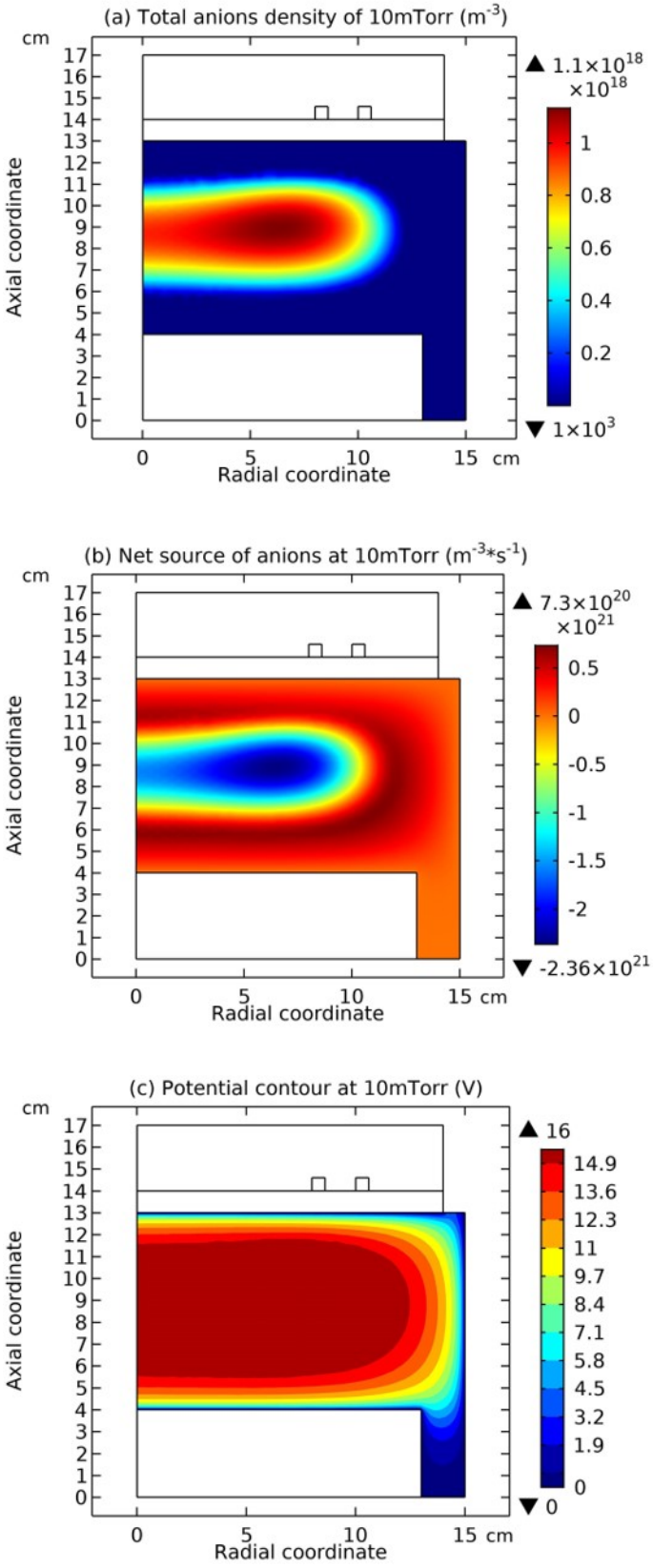

Figure 5. Total anions density (a), net source of anions (b), and plasma potential contour (c) of Ar/SF_6 ICP source, given by the fluid simulation at the pressure of 10 mTorr. The other discharge conditions are 300 W and ten percent of reactive SF_6 content in the gas mixture. The electronegativity of this plasma source is in an order of 100; see Figures 5(a) and 6(c). The anions type and their chemistry can be found in Section 2.1.

 doi:10.20944/preprints202604.0734.v1

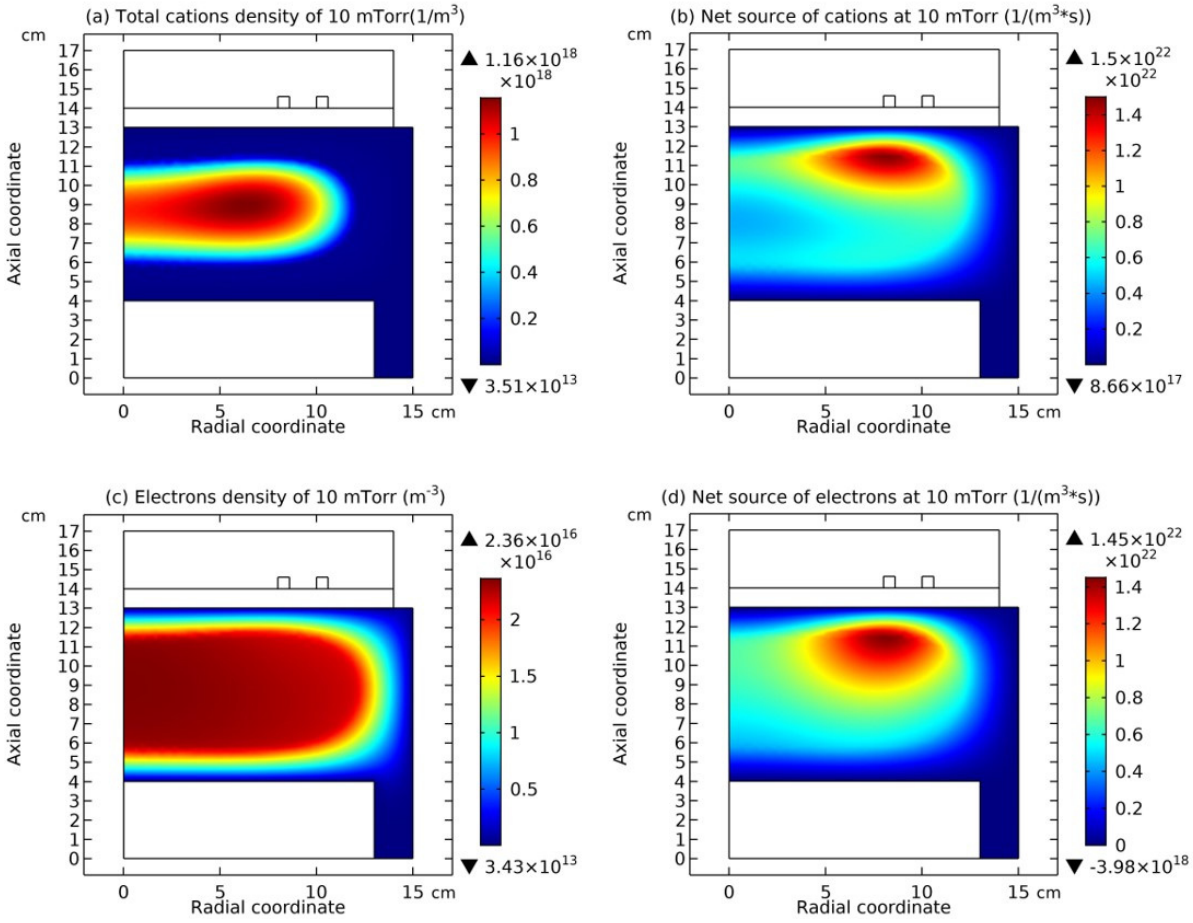

Figure 6. Total cations density (a), net source of cations (b), electrons density (c), and net source of electrons (d) of Ar/SF_6 ICP source, given by the fluid simulation at the pressure of 10 mTorr. The other discharge conditions and the electronegativity of this source are the same as in Figure 5. The cations type and their chemistry can be found in Section 2.1 and the electron chemistry can be found there as well.

3.2. Chemically Ambi-Polar Self-Coagulations of Ions in Highly Electronegative Plasma at High Pressure and Its Implication on the Quantum and Particle Physics

(a) Mixed structure of self-coagulation and ellipse background.

In Figure 7, the summed anions density, the net source of anions, and the electric potential of Ar/SF_6 ICP at the high pressure of 90 mTorr are presented. It is seen from Figures 5(a) and 7(a) as increasing the pressure, the discharge structure of Ar/SF_6 ICP changes. The stratification disappears and a mixed structure of the localized self-coagulation of anions under the coil and the peripherical anions ellipse background, i.e., flattened profile, is formed. Moreover, at the position of coagulated structure, the chemical source of anions in Figure 7(b) is negative, and in Figure 7(c), the profile of potential at the coagulated position is also flat, which implies the free diffusion of anions. So, these two conditions are satisfied again, and the self-coagulation described in Section 2.3c works and the anions coagulates under the coil. Besides, it is noticed the appearance of ellipse profile implies that the discharge shifts from the regime of transport to the regime of chemistry.

 doi:10.20944/preprints202604.0734.v1

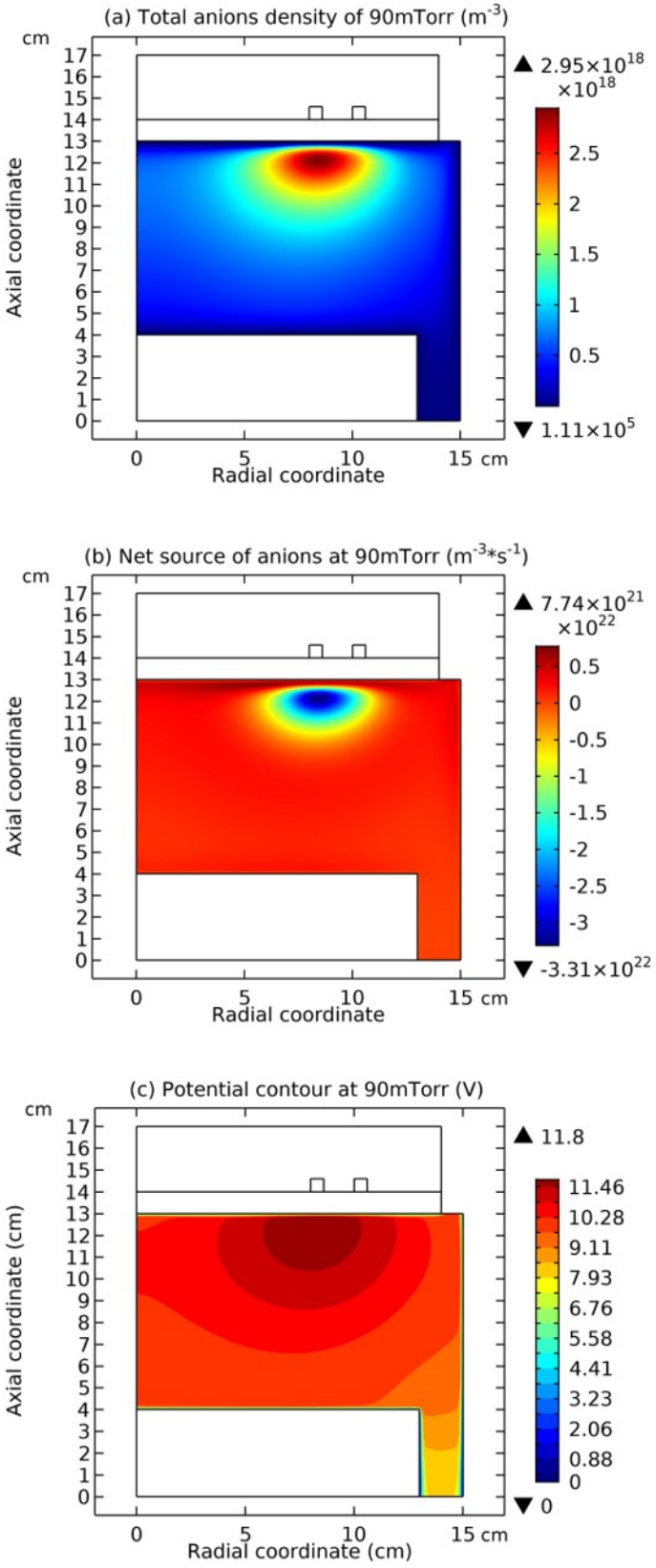

Figure 7. Total anions density (a), net source of anions (b), and plasma potential contour (c) of Ar/SF_6 ICP source, given by the fluid simulation at the pressure of 90 mTorr. The other discharge conditions are the same as in Figure 5. The anions type and the chemistry of them can be found in Section 2.1.

(b) Mass balance of cations at the chemically ambi-polar coagulation scheme.

 doi:10.20944/preprints202604.0734.v1

In Figure 8, the summed cations density and the net source of them in the Ar/SF_6 ICP at the high pressure of 90 mTorr are presented. It is seen that the cations density in Figure 8(a) holds the same profile as anions in Figure 7(a), and meanwhile, in Figure 8(b), the net source of cations in the regime of chemistry exhibits different characteristics, i.e., with a red and positive delta type of chemical source under the coil and the peripherical negative wide-spread type of chemical source. As stated below, at such a characterized profile of chemical source, the cations exhibit the self-coagulation as well, separately.

$$\frac{\partial n_+}{\partial t}+\nabla\cdot\mathbf{\Gamma}_+=\sum\left[R_{G,+}(\mathbf{r})+R_{L,+}(\mathbf{r})\right]. \tag{56}$$

In Equation (56), the general continuity equation of cation density is given. Herein, n_+ are $\mathbf{\Gamma}_+$ the summed cations density and flux, respectively. $R_{G,+}$ and $R_{L,+}$ are the generation and loss sources of them, respectively.

$$\frac{\partial n_+}{\partial t}=R_i\delta(\mathbf{r}-\mathbf{r}_0)-R_l\gamma(\mathbf{r},\mathbf{r}_0). \tag{57}$$

In Equation (57), the specific continuity equation of cation density in the chemical scheme is given, where the mass transport is controlled exclusively by the chemical kinetics and the mass flux is thereby zero. Here, R_i and R_l represent the ionization rate and recombination rate, respectively. They are both assumed constant for simplicity. The introduced functions, $\delta(\mathbf{r}-\mathbf{r}_0)$ and $\gamma(\mathbf{r},\mathbf{r}_0)$, are explained in Equations (58) and (59), respectively.

$$\delta(\mathbf{r}-\mathbf{r}_0)=\begin{cases}\infty, \mathbf{r}=\mathbf{r}_0\\ 0, \mathbf{r}\neq\mathbf{r}_0\end{cases}. \tag{58}$$

$$\gamma(\mathbf{r},\mathbf{r}_0)=\begin{cases}0, \mathbf{r}=\mathbf{r}_0\\ 1, \mathbf{r}\neq\mathbf{r}_0\end{cases}. \tag{59}$$

As illustrated in Equations (58) and (59), $\delta(\mathbf{r}-\mathbf{r}_0)$ is strictly a Dirac function and $\gamma(\mathbf{r},\mathbf{r}_0)$ is a quasi- Step function.

$$R_i\delta(\mathbf{r}-\mathbf{r}_0)-R_l\gamma(\mathbf{r},\mathbf{r}_0)=R_i\delta(\mathbf{r}-\mathbf{r}_0)-n_{+,0}\nu_l\gamma(\mathbf{r},\mathbf{r}_0)=0. \tag{60}$$

In Equation (60), the steady state case of cation continuity equation in the chemical scheme is given. Here, $n_{+,0}$ is the background cation density and ν_l is the recombination frequency of cations with anions.

$$R_i\delta(\mathbf{r}-\mathbf{r}_0)=n_{+,0}\nu_l\gamma(\mathbf{r},\mathbf{r}_0). \tag{61}$$

$$n_{+,0}=\frac{\int R_i\delta(\mathbf{r}-\mathbf{r}_0)\,dV}{\int\nu_l\gamma(\mathbf{r},\mathbf{r}_0)\,dV}=\frac{R_i(\mathbf{r}=\mathbf{r}_0)}{\nu_l(V-\delta V)}. \tag{62}$$

In Equation (61), the balance between the generation and loss rates of cations is given. The two sides of Equation (61) are integrated and then in Equation (63) the background cation density, $n_{+,0}$, is calculated. As seen, it depends on both the localized ionization rate and the widespread recombination frequency. Here, V is the volume of chamber and δV is the occupied volume of localized ionization rate.

$$n_{+,peak}\sim\infty, n_{+,peak}\propto R_i. \tag{63}$$

Finally, in Equation (63), the localized cation density peak, $n_{+,peak}$, is predicted. As seen, it tends to infinite naturally and its magnitude is proportional to the ionization rate logically. To summarize the

 doi:10.20944/preprints202604.0734.v1

self-coagulation of anions in Figure 7 and Section 2.3c and the self-coagulation of cation in Figure 8 and Equations (56)–(63), it is believed a chemically ambi-polar self-coagulation scheme can be defined at the high pressure of 90 mTorr, where both chemistries of anions and cations dominate over the transport. In Figures 9 and 10, it is seen that this type of chemically ambi-polar self-coagulation scheme becomes stronger at the high power, 3600W, and the high pressure, 200mTorr, respectively.

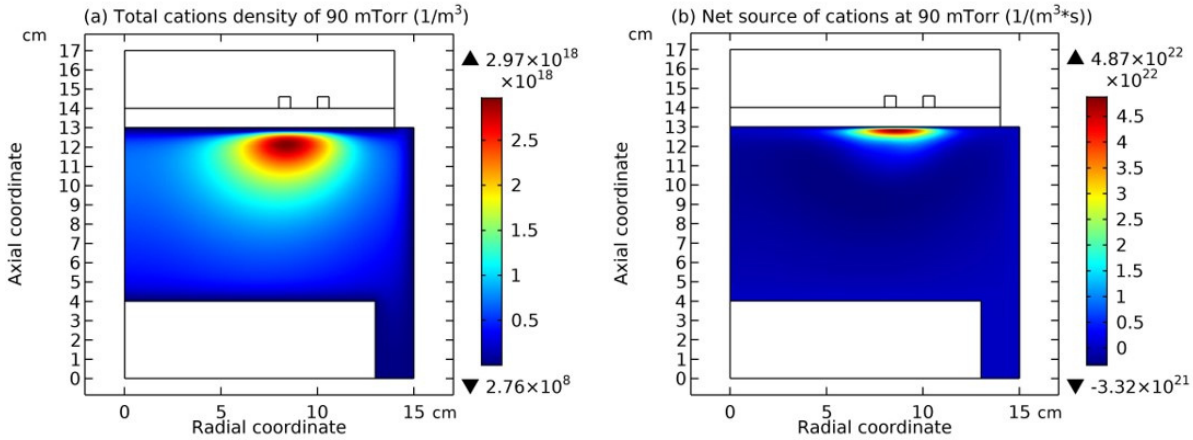

Figure 8. Total cations density (a) and net source of cations (b) of Ar/SF_6 ICP source, given by the fluid simulation at the pressure of 90 mTorr. The other discharge conditions are the same as in Figure 5. The cations type and the chemistry of them can be found in Section 2.1.

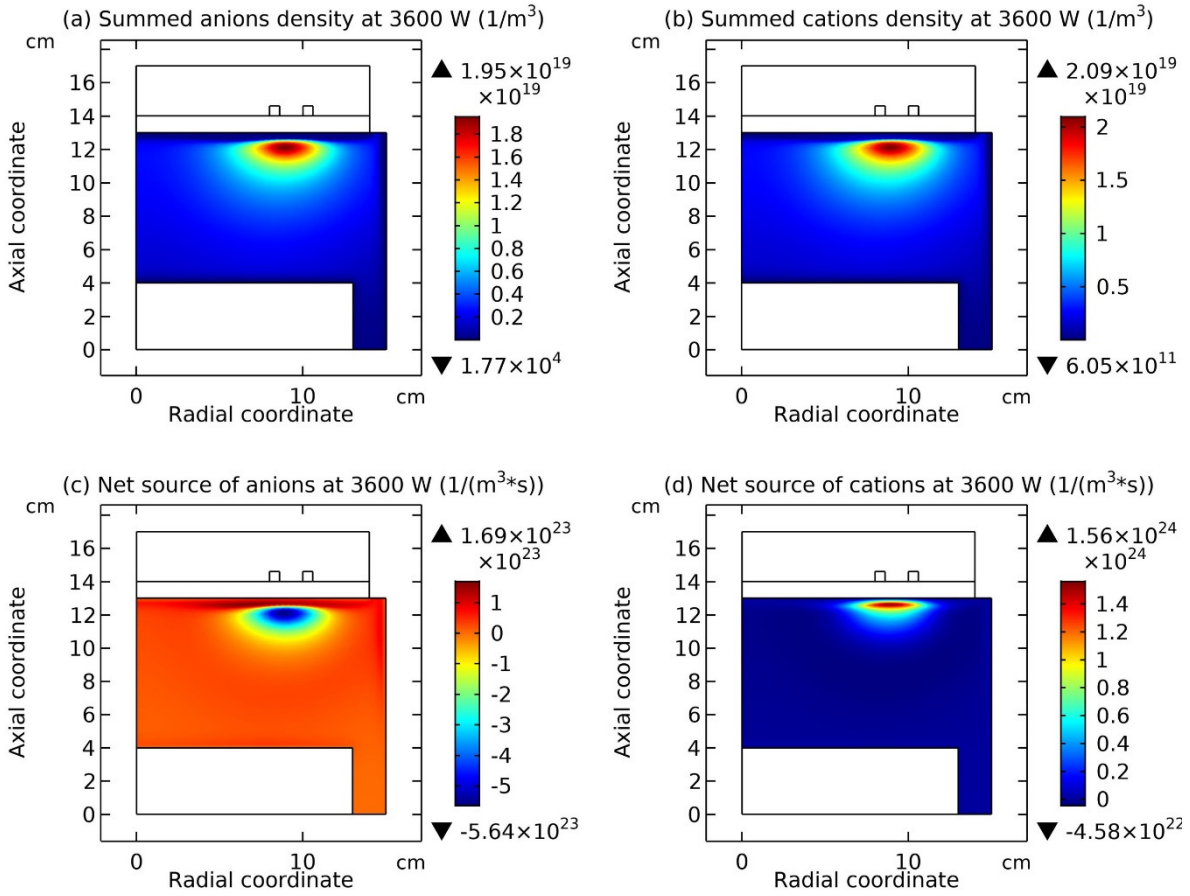

Figure 9. The simulated anions and cations densities (a, b) and simulated chemical sources of them (c, d), at higher power, 3600W, by fluid model. The other discharge conditions are 90 mTorr and 10% SF_6 content.

 doi:10.20944/preprints202604.0734.v1

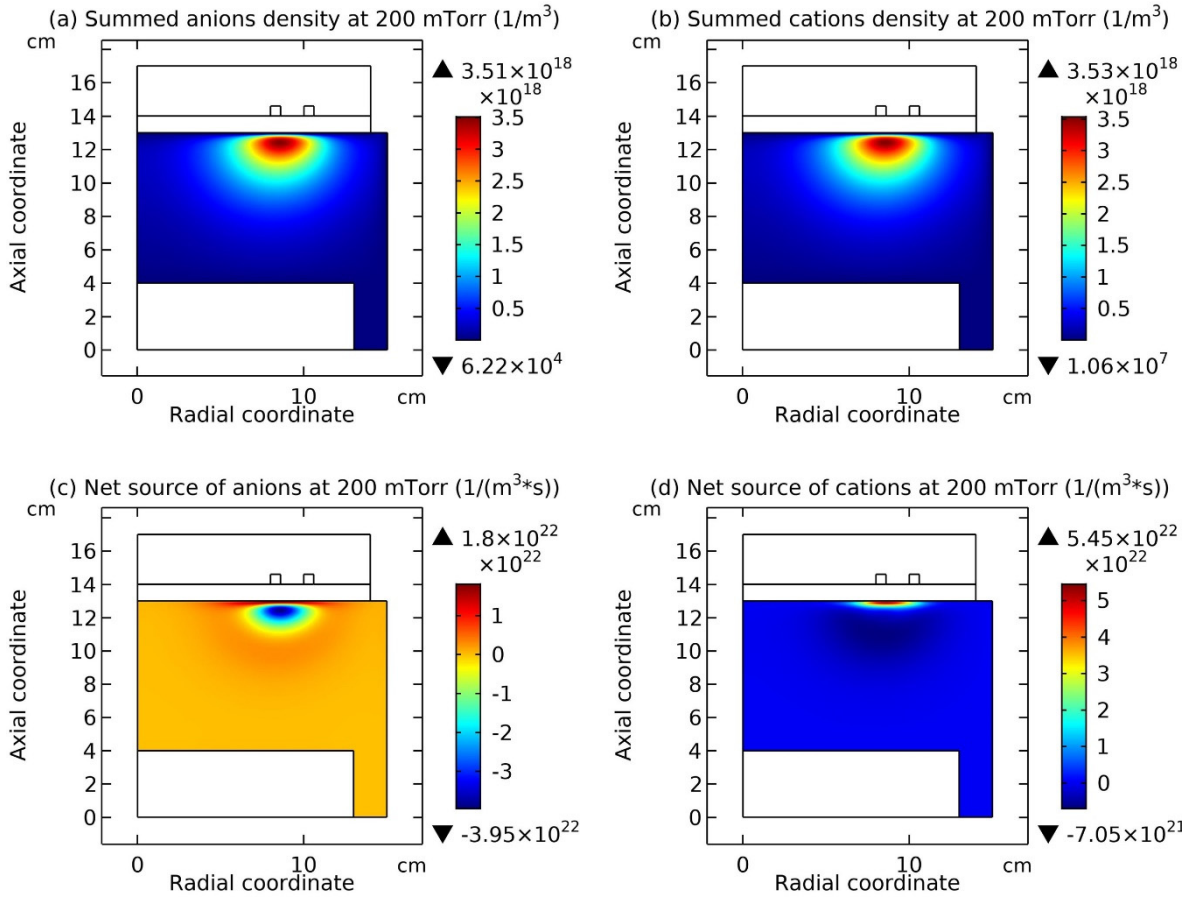

Figure 10. The simulated anions and cations densities (a, b) and simulated chemical sources of them (c, d), at higher pressure, 200mTorr, by fluid model. The other discharge conditions are 300 W and 10% SF_6 content.

(c) Implication of coagulation and ellipse mixed profile on wave-particle duality.

In Ref. [12], it is predicted that the mixed structure of ellipse and self-coagulation represents the wave-particle duality, based on the wave dynamic equation and quasi-particle model equation, when considering the role of inertia term. In the next section, it is further predicted the Schrodinger equation can be used to find out the eigen state of coagulated anions in an assumed semi-circle and infinitely high potential barrier.

(d) Schrodinger equation of anions in the semi-circle infinite high potential barrier

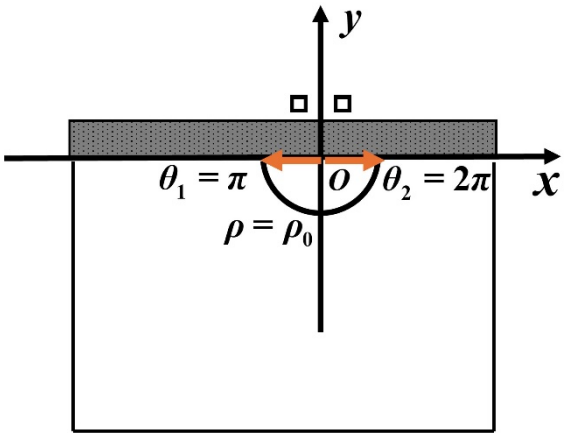

Figure 11. Polar coordinate system for the semi-circle and infinitely high potential barrier model.

 doi:10.20944/preprints202604.0734.v1

In this section, the Schrodinger equation of anions in the semi-circle and infinitely high potential barrier is described and the probabilities of finding the anion particle is given.

$$\text{When } \pi \le \theta \le 2\pi, \rho < \rho_0, \ U(\rho,\theta) = 0. \tag{64}$$

$$\text{When } \pi \le \theta \le 2\pi, \rho \ge \rho_0, U(\rho,\theta) = \infty. \tag{65}$$

In Equations (64) and (65), the potential model is given.

$$\left\{-\frac{\hbar^2}{2m}\left[\frac{1}{\rho}\frac{\partial}{\partial\rho}\left(\rho\frac{\partial}{\partial\rho}\right)+\frac{1}{\rho^2}\frac{\partial^2}{\partial\theta^2}\right]+U(\rho,\theta)\right\}\psi(\rho,\theta) = E\psi(\rho,\theta). \tag{66}$$

In Equation (66), the Schrodinger equation is given. Herein, E is the energy of particle in the potential barrier and $\psi(\rho,\theta)$ is the probability function.

When $\pi \le \theta \le 2\pi, \rho \ge \rho_0$,

$$\left\{-\frac{\hbar^2}{2m}\left[\frac{1}{\rho}\frac{\partial}{\partial\rho}\left(\rho\frac{\partial}{\partial\rho}\right)+\frac{1}{\rho^2}\frac{\partial^2}{\partial\theta^2}\right]+\infty\right\}\psi(\rho,\theta) = E\psi(\rho,\theta) \tag{67}$$

$$\text{So, } \psi(\rho,\theta) = 0. \tag{68}$$

When $\pi \le \theta \le 2\pi, \rho < \rho_0$,

$$-\frac{\hbar^2}{2m}\left[\frac{1}{\rho}\frac{\partial}{\partial\rho}\left(\rho\frac{\partial}{\partial\rho}\right)+\frac{1}{\rho^2}\frac{\partial^2}{\partial\theta^2}\right]\psi(\rho,\theta) = E\psi(\rho,\theta). \tag{69}$$

With the method of variable separation, we have

$$\psi(\rho,\theta) = R(\rho)\Phi(\theta) \tag{70}$$

Substituting $\psi(\rho,\theta)$ in Equation (69) with the above expression of Equation (70), we have

$$-\frac{\hbar^2\rho^2}{2m}\left[\frac{1}{\rho}\frac{\partial}{\partial\rho}\left(\rho\frac{\partial R}{\partial\rho}\right)\frac{1}{R}+\frac{1}{\rho^2}\frac{\partial^2\Phi}{\partial\theta^2}\frac{1}{\Phi}\right] = E\rho^2. \tag{71}$$

Reform Equation (71), we have

$$-\rho^2\left[\frac{1}{\rho}\frac{\partial}{\partial\rho}\left(\rho\frac{\partial R}{\partial\rho}\right)\frac{1}{R}\right]-\frac{2m}{\hbar^2}E\rho^2 = \frac{\partial^2\Phi}{\partial\theta^2}\frac{1}{\Phi}. \tag{72}$$

Introducing the parameter, $-m_\theta^2$, into Equation (72), we have

$$\frac{\partial^2\Phi}{\partial\theta^2}+m_\theta^2\Phi = 0. \tag{73}$$

$$\frac{\partial^2 R}{\partial\rho^2}+\frac{1}{\rho}\frac{\partial R}{\partial\rho}+\left(\frac{2m}{\hbar^2}E-\frac{m_\theta^2}{\rho^2}\right)R = 0. \tag{74}$$

Assume,

$$\mu = \frac{2m}{\hbar^2}E. \tag{75}$$

Then, we have

$$\frac{\partial^2 R}{\partial\rho^2}+\frac{1}{\rho}\frac{\partial R}{\partial\rho}+\left(\mu-\frac{m_\theta^2}{\rho^2}\right)R = 0. \tag{76}$$

Assuming $x = \sqrt{\mu}\rho$, we have

 doi:10.20944/preprints202604.0734.v1

$$\frac{\partial^2 R}{\partial x^2}+\frac{1}{x}\frac{\partial R}{\partial x}+\left(1-\frac{m_\theta^2}{x^2}\right)R=0. \tag{77}$$

As seen, Equation (77) represents the Bessel's equation. The solution of Equation (73) is

$$\Phi = Ce^{im_\theta\theta}. \tag{78}$$

Utilizing the periodical boundary condition, $\Phi(\theta)=\Phi(\theta+2\pi)$, we have

$$e^{i2m_\theta\pi}=1. \tag{79}$$

Hence, the eigen values of introduced parameter are $m_\theta=\pm1,\pm2,\cdots$. So, the Equation (77) is the m_θ integer order Bessel equation. Further utilizing the homogeneous boundary condition of $R(x)$ at $\rho=\rho_0$, we have the another set of eigen values illustrated as

$$\mu=\frac{x_{m_\theta}^2}{\rho_0^2}. \tag{80}$$

Here, x_{m_θ} represents all the zero points of m_θ order Bessel function. By correlating Equation (75), we finally have the eigen energy as follows,

$$E=\frac{\hbar^2 x_{m_\theta}^2}{2m\rho_0^2}=\frac{\hbar^2}{2m}x_{m_\theta}^2\frac{1}{\rho_0^2}. \tag{81}$$

It is seen that the energy level of particle in such a barrier depends on the value of m_θ. When the order number of Bessel function, i.e., the value of m_θ, is fixed, the energy interval of two energy levels is determined by the deduct of squares of two adjacent zero points of m_θ order Bessel function, illustrated below,

$$\nabla E=\frac{\hbar^2\left(x_{m_\theta,2}^2-x_{m_\theta,1}^2\right)}{2m\rho_0^2}=\frac{\hbar^2}{2m}\left(x_{m_\theta,2}^2-x_{m_\theta,1}^2\right)\frac{1}{\rho_0^2}. \tag{82}$$

Since the Planck's constant, $\hbar$, is quite small and the square deduct of zero points of Bessel's function is limited value, the energy interval will tend to zero if the size of semi-circle and infinitely high potential barrier is large enough, like in an order of centimeter as designed in the fluid simulation of Ar/SF_6 ICP. As the energy level tends to zero in the size of centimeter, the quantum scheme transitions to the continuity scheme, and the probability of finding the particle in the potential barrier is one.

(e) Implication on particle physics, β decay.

In this sub-section, the implication of self-coagulation and related hierarchy on the decay in nucleus is elaborated. In Ref. [12], the two main structures of hierarchy at the high pressure of 90 mTorr, coagulated body and ellipse background, are correlated to the neutron and proton models, respectively, since the blue sheath that connects the two structures is expressed with the Yukawa potential[18], which represents a meson[19]. Herein, it is believed that the β and β^+ decays occurring in the nucleus[20] as listed in Table 1, can be interpreted by a change of coil position from the top to bottom, verse vice, as illustrated by Figures 12–15. In Figures 12 and 14, the coil is on the top, while in Figures 13 and 15, the coil is on the bottom, i.e., a reversed chamber that is clockwise rotated π. In Figures 12 and 13, the summed anions density, summed cations density, net source of anions, net source of cations, electron density, and electric potential, at the top and bottom coil positions are plotted, respectively. And in Figures 14 and 15, the summed neutrals and molecules, at the two coil positions, are plotted, respectively. It's analyzed from the Figures 12(a, b), and 13(a, b), as the coil is changed from the top to the bottom, the neutron under the coil turns into the proton. Meanwhile, the

 doi:10.20944/preprints202604.0734.v1

electron released in this β decay is represented by the coagulated electrons in Figure 13 (e), and the anti-neutrino released is represented by the coagulated neutrals in Figure 15 (a).

Table 1. Two types of β decay.

β decay	Neutron → proton + electron + anti-neutrino
β^+ decay	Proton → neutron+ positron + neutrino

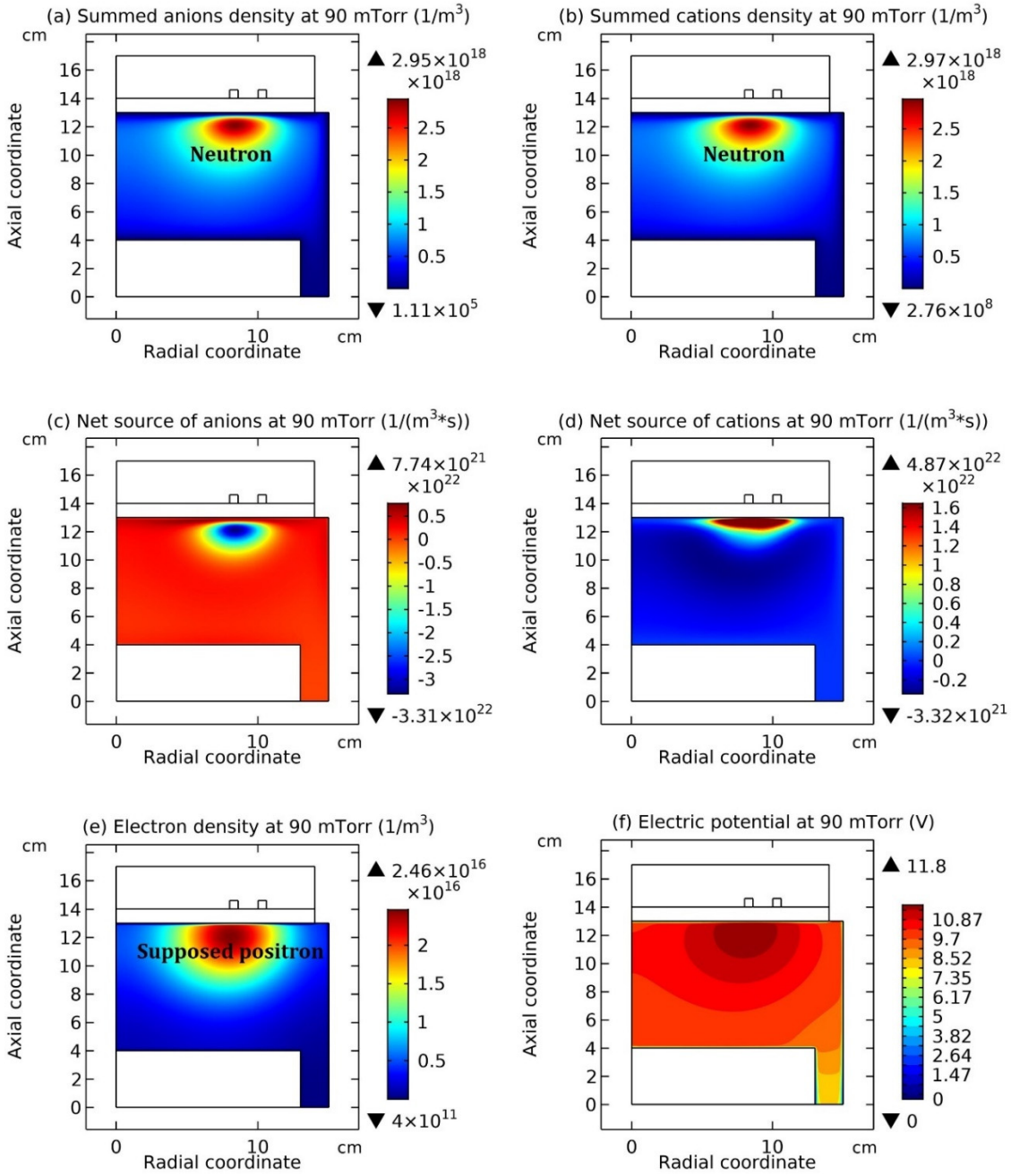

Figure 12. Total anions density (a), total cations density (b), net source of anions (c), net source of cations (d), electrons density (e), and plasma potential contour (f) of Ar/SF_6 ICP source in the normal chamber, given by the fluid simulation at the pressure of 90 mTorr. The other discharge conditions are the same as in Figure 5. Herein, the anion and cation types and their corresponding chemistries considered can be found in Section 2.1.

 doi:10.20944/preprints202604.0734.v1

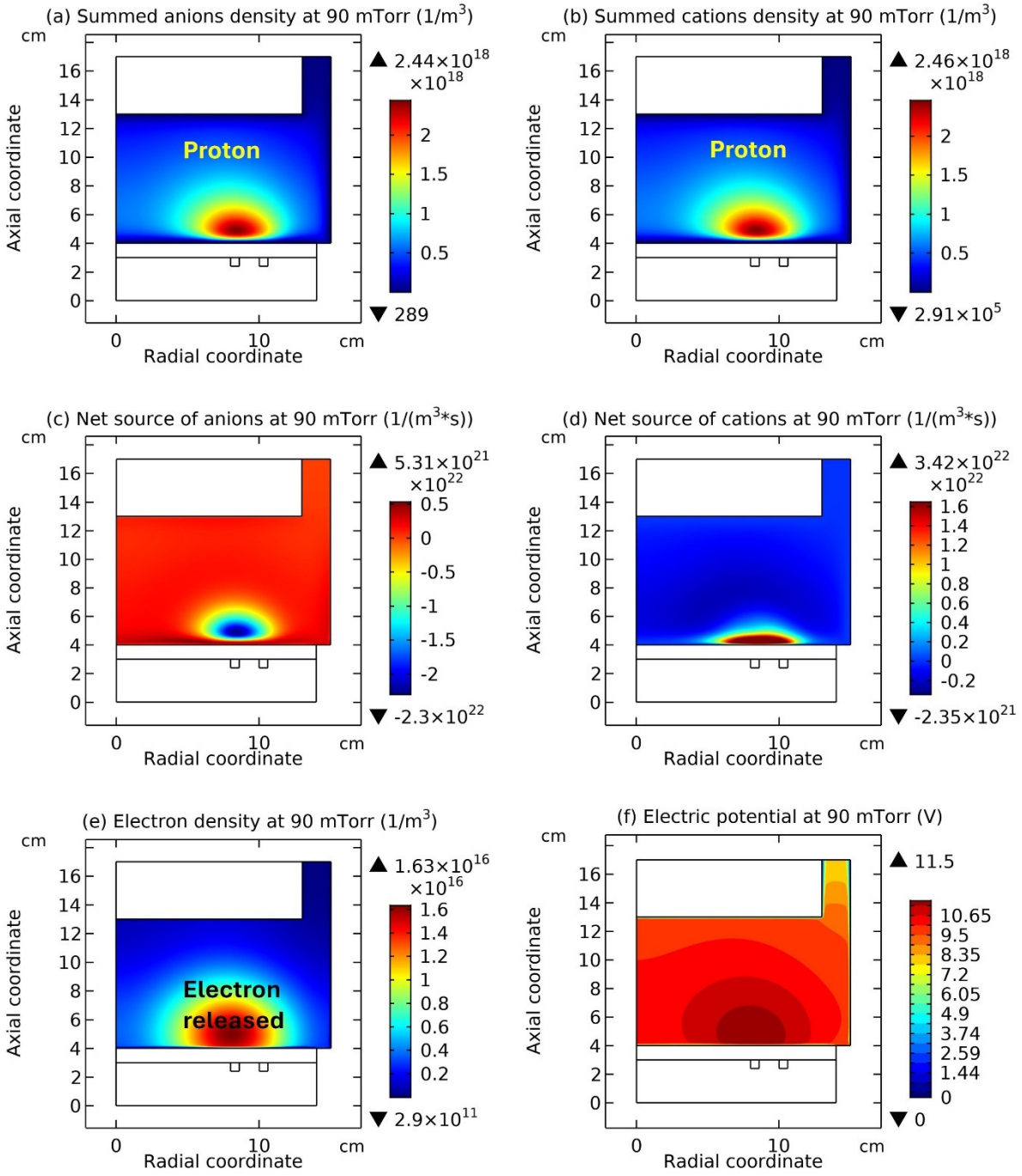

Figure 13. (a) summed anions density, (b) summed cations density, (c) net source of anions, (d) net source of cations, (e) electron density, and (d) electric potential of Ar/SF6 ICP at 90 mTorr and in the reversed ICP chamber. The other discharge conditions are the same as Figure 5. Herein, the anion and cation types and their corresponding chemistries considered can be found in Section 2.1.

Reversely, as the coil is changed from the bottom to the top, i.e., seen from Figure 13 to Figure 12, the proton in Figure 13 (a, b) turns into the neutron under the coil in Figure 12(a, b). Accordingly, the supposed positron is released, which is represented by the coagulated electrons, as shown in Figure 12 (e), and the neutrino released is represented by the coagulated neutrals under the coil in Figure 14 (a). It's noted the positron is presently not included in the simulation, and we have tried to include the positron and photon as species in the present simulation, but all failed lastly due to the lack of self-consistency. However, in the next two Sections 3.3 and 3.4, it is predicted that the mono-polar mass, including the electron and positron, can be self-coagulated, and even the non-polar mass, e.g., metastable argon, can be self-coagulated too, which somehow represent the positron (was is

 doi:10.20944/preprints202604.0734.v1

existed) and the neutrino. In the real β^- and β^+ decays in the nucleus, all the needed components, i.e., neutron, proton, electron, positron, neutrino, and anti-neutrino are existed. In the present simulation environment, only five components are involved, and the positron is excluded due to its strict condition for production. Nevertheless, it is believed was it included in the present framework, can it be self-coagulated, since self-coagulation does no requires a specialty on the polarity, but a special requirement on chemical reaction source term; see Sections 3.3 and 3.4 for reference.

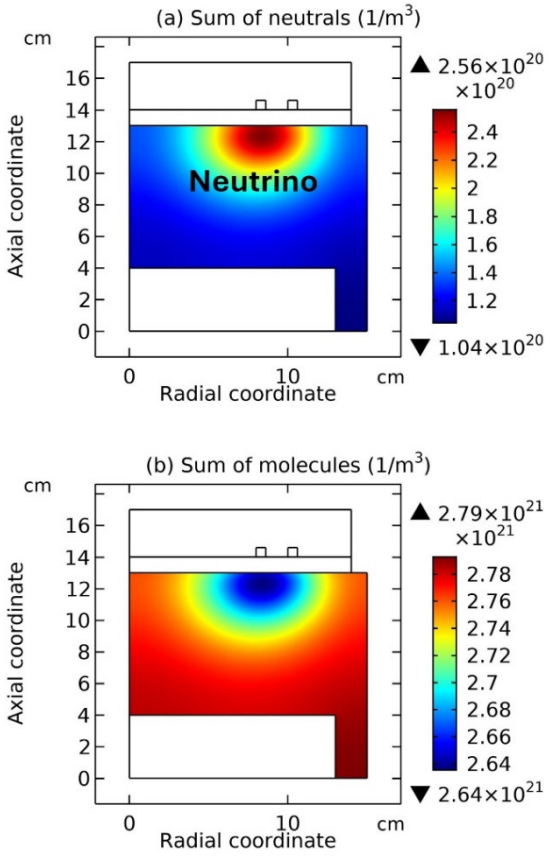

Figure 14. (a) Sum of neutral densities, including SF_5, SF_4, SF_3, SF_2, SF, S, F, F_2, Ars, and (b) sum of molecule densities, including SF_6 and Ar, in the normal chamber and at the pressure of 90mTorr. The other discharge conditions are the same as in Figure 5. Here, Ars represents the metastable argons.

Besides, the neutrino holds the left-hand spin orientation, and the anti-neutrino holds the right-hand spin orientation[21]. Assume the neutrino model in Figure 14(a) flights outside, then its spin is left-handed since the left side is faced with the space but the right side is against the wall. Moreover, assume the anti-neutrino model in Figure 15(a) flights outside as well, then its spin is right-handed, since the right side is against the wall but the left side is faced with the space. The assumed flighting directions of neutrino in Figure 14(a) and of anti-neutrino in Figure 15(a) are both out of page but the spin orientations of them are contradictory, because of the asymmetry caused by the π clockwise rotation of chamber. In Figure 16, more details of neutrino and anti-neutrino spin characteristics and the origin of spin, coil current and its azimuthal rotation are given. The whole story of β^- and β^+ decays depicted herein originates from the asymmetry, i.e., the coil that represents the particle coagulation position changes from the top to the bottom.

 doi:10.20944/preprints202604.0734.v1

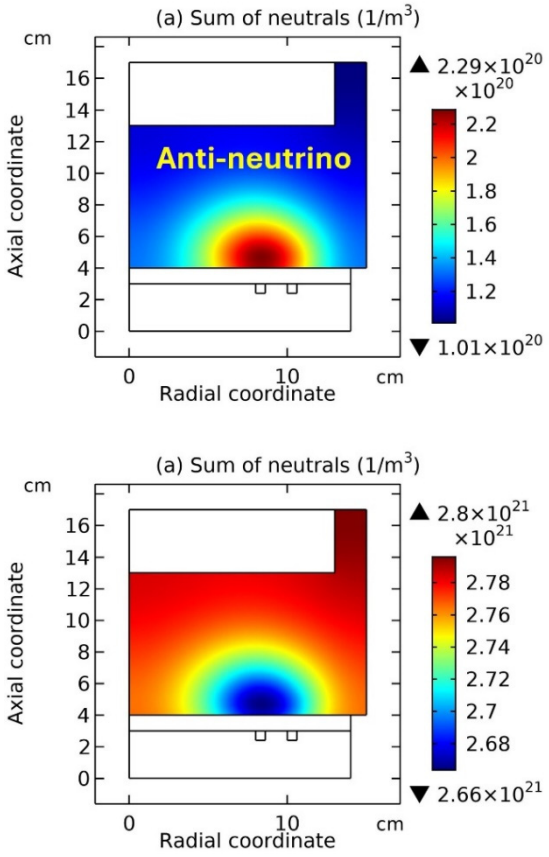

Figure 15. (a) Sum of neutral densities, including SF_5, SF_4, SF_3, SF_2, SF, S, F, F_2, Ars, and (b) sum of molecule densities, including SF_6 and Ar, in the reversed chamber and at the pressure of 90 mTorr. The other discharge conditions are the same as in Figure 5. Here, Ars represents the metastable argons.

The view of three-dimension chamber configuration and the cylindrical symmetry of simulation assumed are needed to understand the asymmetry of chamber clockwise rotation in Figure 16. In the upper panel of Figure 16(a), the corresponding left profile of simulated intersection of chamber in the radial and axial dimensions that is always presented on the right side, is duplicated based on the cylindrical symmetry, when the coil is at the top. Accordingly, in the down panel of Figure 16(a), the corresponding left profile of right-side simulated intersection in the two dimensions is duplicated as well based on the symmetry, when the coil is at the bottom. In the upper and left panel of Figure 16(a) the term, A terminal of coil, is defined above the dielectric window, while in the upper and right panel of Figure 16(a) the term, B terminal of coil, is defined above the dielectric. And in the upper panel of Figure 16(b), assume the coil current flows as illustrated, A terminal in and B terminal out, at the moment of chamber clockwise rotation. Then, after this clockwise rotation, in the down panel of Figure 16(a), B terminal of coil is shifted into the left profile and A terminal of coil is shifted into the right profile. Furthermore, refer to the coil current flowing direction after the clockwise rotation in the down panel of Figure 16(b) and it changes into, A terminal out and B terminal in, due to the asymmetry introduced. Namely, the coil current flow changes its direction when it rotates a π. Actually, the right two sub-panels of Figure 16(a) correspond to the Figure 14(a) and Figure 15(a), separately. Moreover, the left two sub-panels of Figure 16(a) correspond to the left-hand spin of neutrino and the right-hand spin of anti-neutrino, respectively, but with coil current flowing into the page.

 doi:10.20944/preprints202604.0734.v1

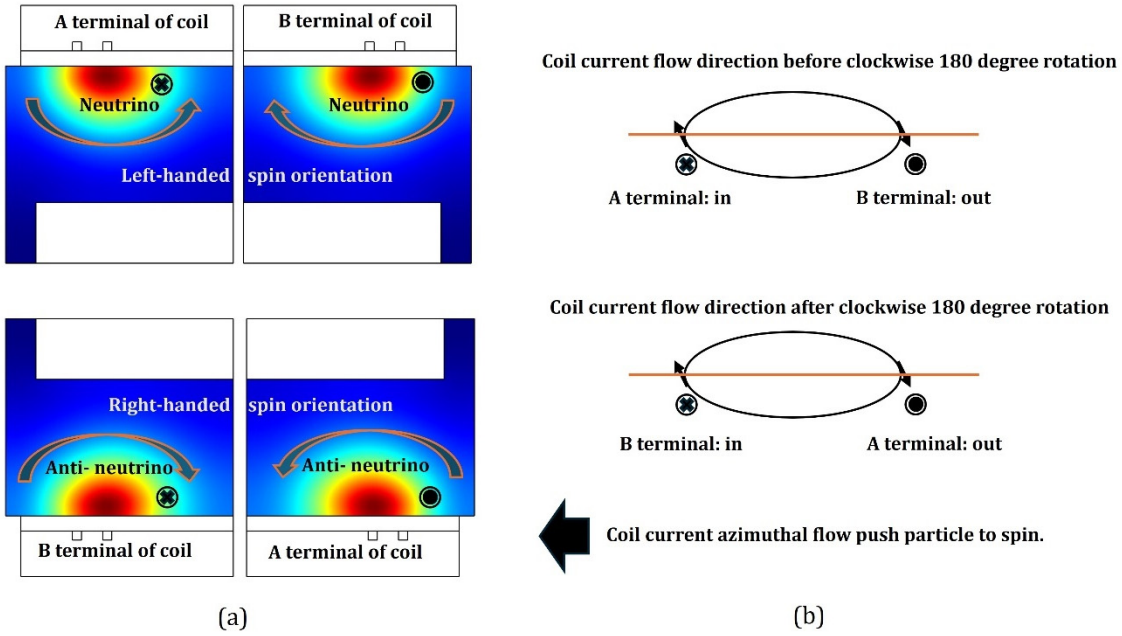

Figure 16. (a) Neutrino and anti-neutrino spin characteristics and (b) the origin of spin: coil current and its azimuthal rotation.

It is believed that in Ref. [17], at the self-coagulation role that condenses scattering mass into particles, the macroscopic plasma mass does not hold spin property, but has the self-diffusion or strong ambi-polar diffusion to constitute a dynamic balance between the mass compression and dispersion. Nevertheless, for microscopic plasma mass, such as neutrino and anti-neutrino, it is believed that self-coagulation exists as well to sustain the particle property, but transport phenomena does not exist anymore due to the tiny mass, size and space. Instead, the spin is needed to construct the dynamic balance of mass compression and dispersion. The predictions in Figure 16 about the spin properties are based on the macroscopic view; nevertheless, this macroscopic analysis based on the transport is in accord to the real spin property, again illustrating that the microscopic quantum property will comply with the real body particle, along with the space size increasing. Besides, the thereby depicted "spins" in Figure 16(a) all orient toward the space, which validates that a spin in the microscopic particles is to abandon mass to the space, so against the self-coagulation that accumulate mass from the space. Lastly, the summed molecules, SF_6 and Ar in Figures 14(b) and 15(b), are not coagulated but sunk, because of a mass balance that all plasma species, e.g., electrons, anions, cations, neutrals, and even further the positron, all arise from the mixed feedstock gases.

3.3. Monopolar Self-Coagulation of Electrons in Electronegative Plasma at High Pressure and Its Implication on Self-Coagulation of Positron Model

In Figure 17, the electron density, net source of electrons, and the net source of electrons with a numerical truncation in the figure legend in the Ar/SF_6 ICP source at 90 mTorr are presented. Compare the net source of electrons before and after the numerical truncation in Figure 17(b,c), and it is seen that besides for the red and positive electron production (ionization) source under the coil, the peripherical blue and negative electron consumption (attachment) source is clear. The *inner red* and *out blue* profile feature of electron net source characterizes the coagulated density distribution of electron, as illustrated by Equations (56)-(63), but under the scope of mono-polar self-coagulation. In one of our other articles [22], it is revealed the discharge of Ar/SF_6 ICP is relatively independent at the high pressure of 90 mTorr, which ensures here the monopolar self-coagulation of electron, against the ambi-polar self-coagulation of ions. But note that they are both chemical type of coagulation, no matter the mono- or ambi- polar type. Compare the electron and cation net chemical sources in Figure

 doi:10.20944/preprints202604.0734.v1

17(b) and 8(b), and it is found the negative source of electron is less pronounced and so the coagulated electron density is not that dense as ions. In addition, as mentioned in Section 3.2e, since the mono-polar self-coagulation of electron does not require the negative polarity, but its intrinsic chemical property, it is predicted the positron density if accompanied with the *inner red* and *out blue* profile feature of net source, will self-coagulate as well, which supplements the analysis of β^+ decay in Section 3.2e

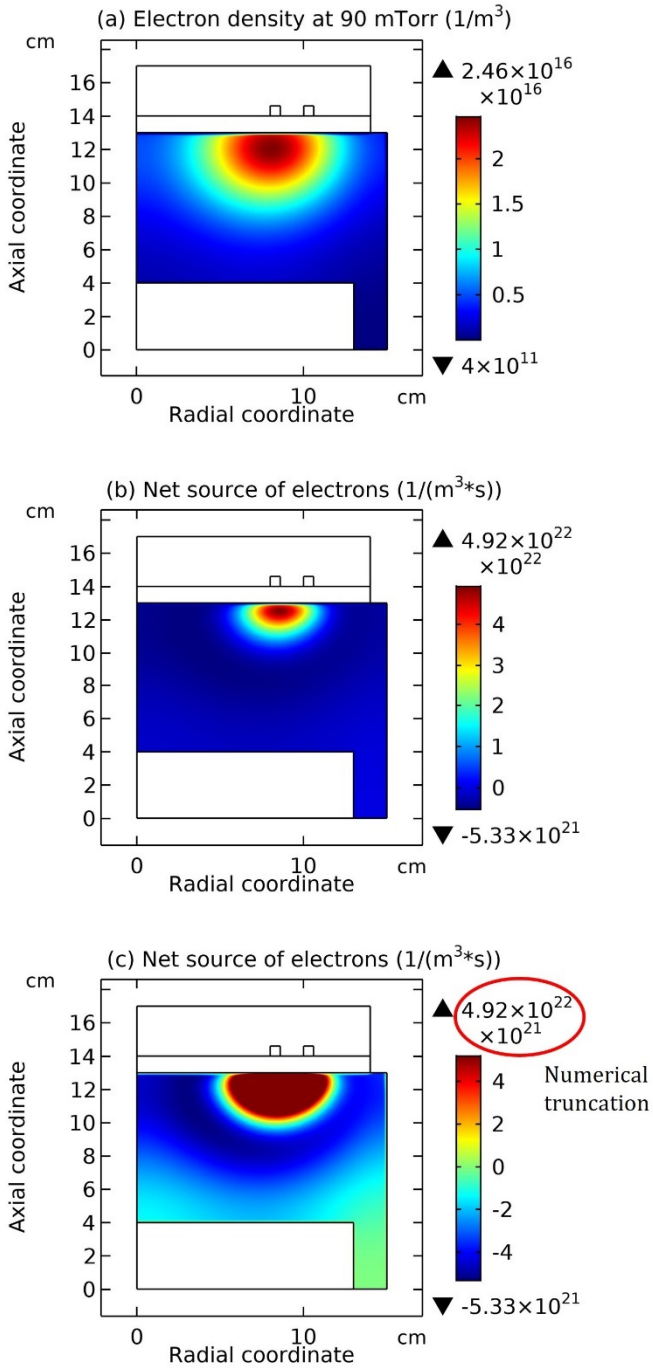

Figure 17. (a) Electron density, (b) net source of electrons, and (c) still net source of electrons but with a numerical truncation in the legend for the Ar/SF_6 ICP source, given by the fluid simulation at the pressure of 90 mTorr. The other discharge conditions are the same as in Figure 5. The numerical truncation in the maximum legend of electron net source in Figure 17(c) is to express its peripherical negative chemical source.

 doi:10.20944/preprints202604.0734.v1

3.4. Non-Polar Self-Coagulation of Neutral Species in Electropositive Plasma and Its Implication on Neutrino Model

In Figure 18, the metastable argon densities in an electropositive Ar ICP source at the pressure set of 20mTorr, 100mTorr, 200mTorr, 300mTorr, 400mTorr, and 500mTorr are presented. Correspondingly, the net sources of metastable argon at the above pressures are plotted in Figure 19. It is seen that at the low pressure of 20mTorr, the metastable argon density profile in Figure 18(a) is parabolic due to the transport dominance at low pressure, like the parabola analytic theory of electronegative plasma in Section 2.3a. Actually, it is quite easy to construct the parabola theory of metastable argon in the electropositive plasma source, as illustrated by the Equations (83)- (85). Herein, n_m, $\mathbf{\Gamma}_m$, R_m, and D_m are the metastable density, flux, source term, and diffusivity, respectively.

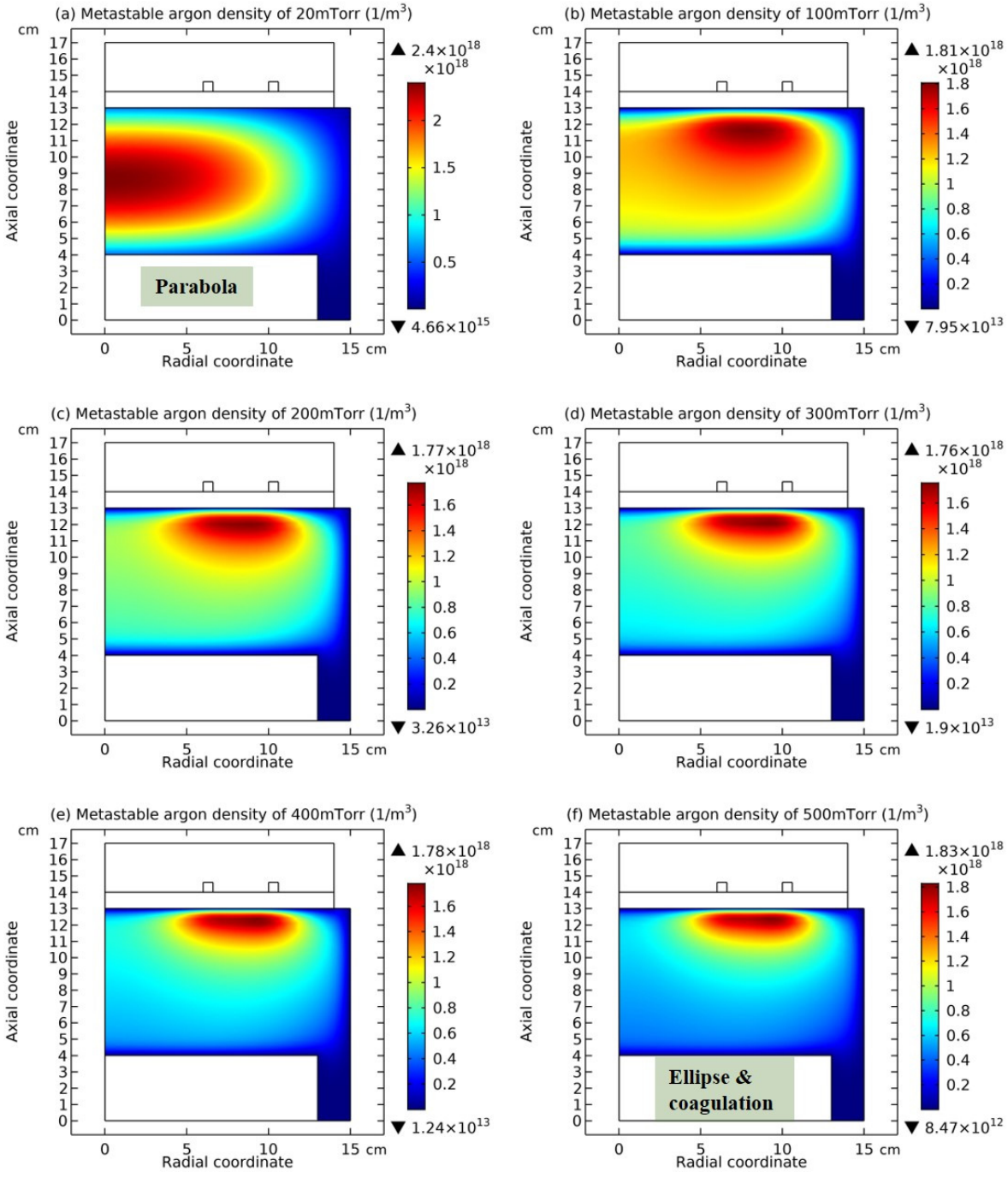

 doi:10.20944/preprints202604.0734.v1

Figure 18. Density of metastable argon atoms at (a) 20 mTorr, (b) 100 mTorr, (c) 200 mTorr, (d) 300 mTorr, (e) 400 mTorr, and (f) 500 mTorr in the Ar ICP source, given by the fluid simulations of argon ICP with the Comsol software, at the power of 300 W.

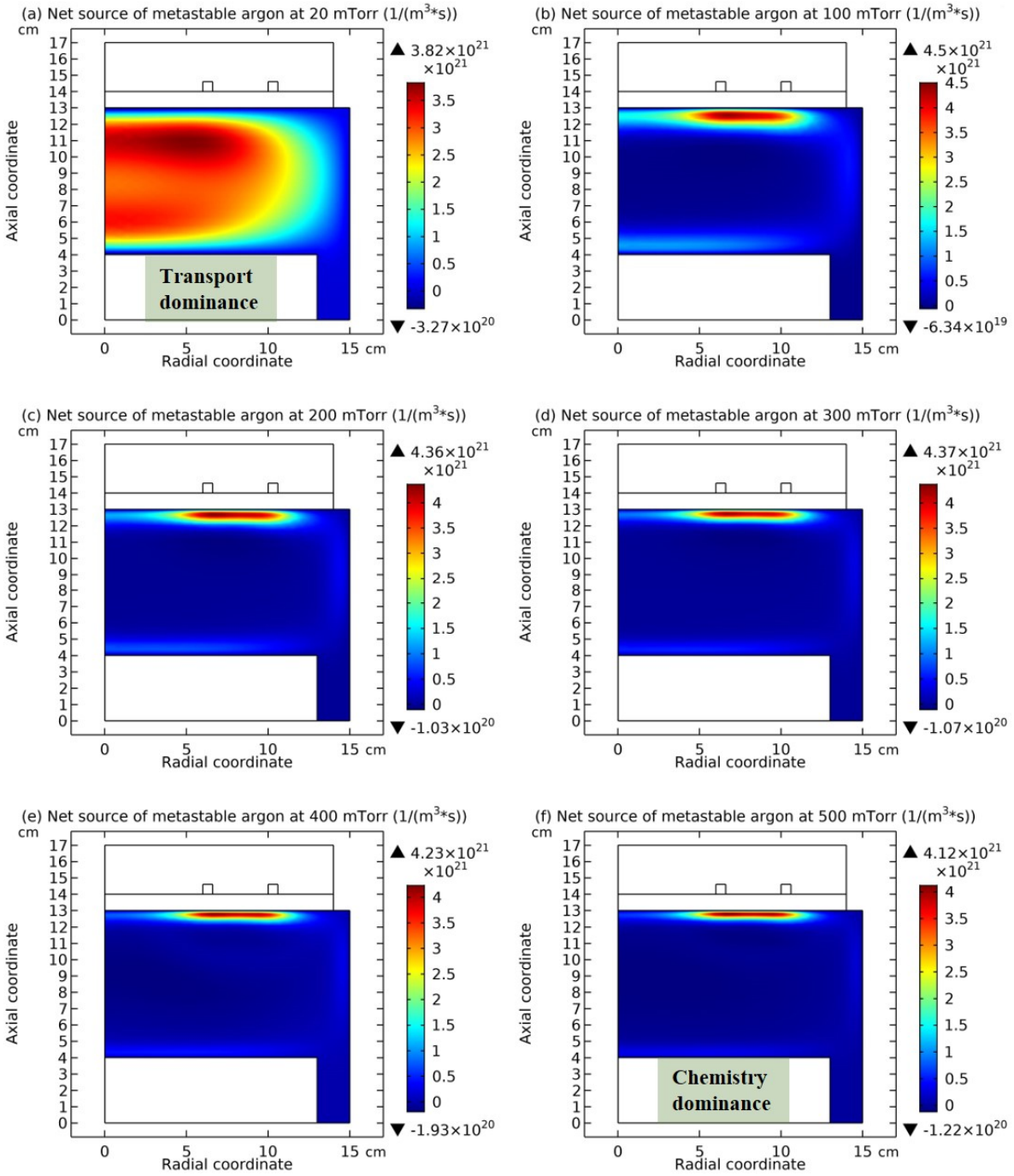

Figure 19. Net source of metastable argon atoms at (a) 20 mTorr, (b) 100 mTorr, (c) 200 mTorr, (d) 300 mTorr, (e) 400 mTorr, and (f) 500 mTorr in the Ar ICP source, given by the fluid simulations at the power of 300 W with the Comsol software. The chemistry of metastable can be found in Section 2.1.

$$\frac{\partial n_m}{\partial t} + \nabla \cdot \mathbf{\Gamma}_m = R_m, \tag{83}$$

$$\frac{\partial n_m}{\partial t} \to 0, \nabla \cdot \mathbf{\Gamma}_m = -D_m \nabla^2 n_m \to -D_m \frac{\partial^2 n_m}{\partial x^2}, R_m \to const, \tag{84}$$

 doi:10.20944/preprints202604.0734.v1

$$\frac{\partial^2 n_m}{\partial x^2}+\frac{R_m}{D_m}=0. \tag{85}$$

In Equation (84), the net source of metastable argon at the low pressure of 20mTorr is taken as constant, which implies the regime of transport dominance, as illustrated in Figure 19(a). In Figure 18(b-f), it is seen the idealized and mixed discharge structure of self-coagulation of metastable argon density under the coil and the peripherical ellipse background is gradually formed as increasing the pressure up to 500mTorr. This mixed structure is similar to the profiles of ions and electrons in Ar/SF_6 ICP source in Figures 7(a), 8(a), and 17(a). Correspondingly, the net source of metastable argon at 500mTorr in Figure 19(f) also exhibit the inner red and out blue profile feature, like the net sources of ions and electrons in Ar/SF_6 ICP source at 90mTorr in Figures 7(b), 8(b), and 17(b). As predicted by the ellipse theory in Section 2.3b, the appearance of ellipse profile implies the high-pressure regime of chemistry dominance over the transport regime of low-pressure case, as illustrated in Figure 19(f, a), respectively. Actually, the initial shift of metastable density peak from the chamber center to the coil upon increasing the pressure from 20mTorr to 100mTorr already implies that the chemistry starts to play roles in forming the discharge structure, and so except for the net source of metastable of 20mTorr case in Figure 19(a), all the other chemical source of metastable in Figures 19(b)-(f) holds the similar structure, *inner red and out blue* characterized. So, it is concluded the self-coagulation of mass is universal, which includes the physically ambi-polar type, chemically ambi-polar type, mono-polar type and the non-polar type. And the last one represents the coagulation of neutrino, as an idea that is already utilized in Section 3.2e.

3.5. Self-Coagulation of Thermal Energy in Electropositive Plasma and Its Implication on Photon Model

(a) Thermodynamic temperature and mean energy equations of electron.

$$\begin{aligned}&\frac{\partial n_e}{\partial t}\cdot\frac{3}{2}kT_e+\frac{3}{2}k\frac{\partial T_e}{\partial t}\cdot n_e=-\frac{5}{2}\nabla\cdot\boldsymbol{\Gamma}_e\cdot kT_e-\frac{5}{2}\boldsymbol{\Gamma}_e\cdot k\nabla T_e\\&+\frac{5}{2}\nabla\left(\frac{n_e kT_e}{m_e\nu_{en}}\right)\cdot\nabla\left(kT_e\right)+\frac{5}{2}\frac{n_e kT_e}{m_e\nu_{en}}\nabla^2\left(kT_e\right)-e\boldsymbol{\Gamma}_e\cdot\mathbf{E}-E_e+P_{ind},\end{aligned} \tag{86}$$

$$\begin{aligned}&\left[R_e-\nabla\cdot\boldsymbol{\Gamma}_e\right]\cdot\bar{\varepsilon}+\frac{\partial\bar{\varepsilon}}{\partial t}\cdot n_e=-\frac{5}{2}\nabla\cdot\boldsymbol{\Gamma}_e\cdot kT_e-\frac{5}{2}\boldsymbol{\Gamma}_e\cdot k\nabla T_e\\&+\frac{5}{2}\nabla\left(\frac{n_e kT_e}{m_e\nu_{en}}\right)\cdot\nabla\left(kT_e\right)+\frac{5}{2}\frac{n_e kT_e}{m_e\nu_{en}}\nabla^2\left(kT_e\right)-e\boldsymbol{\Gamma}_e\cdot\mathbf{E}-E_e+P_{ind},\end{aligned} \tag{87}$$

$$\begin{aligned}&\frac{\partial\bar{\varepsilon}}{\partial t}\cdot n_e=-R_e\bar{\varepsilon}-E_e+P_{ind}+kT_e(-\nabla\cdot\boldsymbol{\Gamma}_e)+\frac{5}{2}k\nabla T_e\cdot\left(-\boldsymbol{\Gamma}_e\right)+\frac{5}{2}\nabla\left(\frac{n_e kT_e}{m_e\nu_{en}}\right)\cdot\nabla\left(kT_e\right)\\&+\frac{5}{2}\frac{n_e kT_e}{m_e\nu_{en}}\nabla^2\left(kT_e\right)-e\boldsymbol{\Gamma}_e\cdot\mathbf{E}\end{aligned} \tag{88}$$

$$\begin{aligned}&\frac{\partial\bar{\varepsilon}}{\partial t}-\frac{5}{2}\frac{kT_e}{m_e\nu_{en}}\nabla^2\left(kT_e\right)=-\frac{R_e}{n_e}\bar{\varepsilon}-\frac{E_e}{n_e}+\frac{P_{ind}}{n_e}-\frac{kT_e\nabla\cdot\boldsymbol{\Gamma}_e}{n_e}-\frac{5}{2}\frac{k\nabla T_e\cdot\boldsymbol{\Gamma}_e}{n_e}\\&+\frac{5}{2n_e}\nabla\left(\frac{n_e kT_e}{m_e\nu_{en}}\right)\cdot\nabla\left(kT_e\right)-\frac{e\boldsymbol{\Gamma}_e\cdot\mathbf{E}}{n_e},\end{aligned} \tag{89}$$

 doi:10.20944/preprints202604.0734.v1

$$\frac{\partial \bar{\varepsilon}}{\partial t}-\frac{5}{3}\frac{kT_e}{m_e\nu_{en}}\nabla^2\bar{\varepsilon}=-\frac{R_e}{n_e}\bar{\varepsilon}-\frac{E_e}{n_e}+\frac{P_{ind}}{n_e}-\frac{kT_e\nabla\cdot\boldsymbol{\Gamma}_e}{n_e}-\frac{5}{2}\frac{k\nabla T_e\cdot\boldsymbol{\Gamma}_e}{n_e}$$
$$+\frac{10}{9n_em_e\nu_{en}}\nabla\left(n_e\bar{\varepsilon}\right)\cdot\nabla\left(\bar{\varepsilon}\right)-\frac{e\boldsymbol{\Gamma}_e\cdot\mathbf{E}}{n_e}. \quad (90)$$

As mentioned before in Section 2.2, the fluid model of pure argon ICP source with self-written code is used to analyze the thermal energy self-coagulation scheme. Based on the electron continuity equation, flux, energy density equation and energy flux in Equations (8), (9), (11) and (12), respectively, the electron mean energy equation, defined as $\bar{\varepsilon}=\frac{3}{2}kT_e$, can be obtained through the deduction of Equations (86)-(90). In the final electron mean energy equation, i.e., Equation (90), at the left side, the inertia term and the thermal conductivity term are presented, and at the right size, all the summed terms represent an effective electron mean energy source term.

(b) Energy self-coagulation and its Implication on photon model.

In Figure 20, the schematic diagram of argon ICP chamber used in the fluid simulation of self-written code and the cylindrical coordinate system orientations are presented, respectively. At a finer mesh used in the numerical scheme, in Figure 21, the electron mean energy in the Ar ICP source is peaked under the coil and close the cylindrical axis, and its effective net source, as presented by the right side of Equation (90), is coincidently sunk at the peak position of mean energy. The energy self-coagulation is therefore defined since the source is negative and the thermal conductivity in the second term at the left side of Equation (90) is essentially the free diffusion of energy, as represented by the product of thermal conductivity coefficient and the second order derivative of electron mean energy. The thermal energy self-coagulation of electron thereby implies a photon model which contains energy but without mass, since the electron continuity equation has been deleted somehow from the energy density equation, as illustrated in Equations (86)-(90). In the analytical theory of Section 2.3c, the mass density used in the quasi- Helmholtz equation can be replaced by the thermal energy of electron. Besides, the effective source term of electron mean energy in Equation (90) contains rich information of electron density, which may explain why at suitable condition, the photon can be quenched into the electron and positron pair [23], was the energy of self-coagulation in the environment of positron can be built as well.

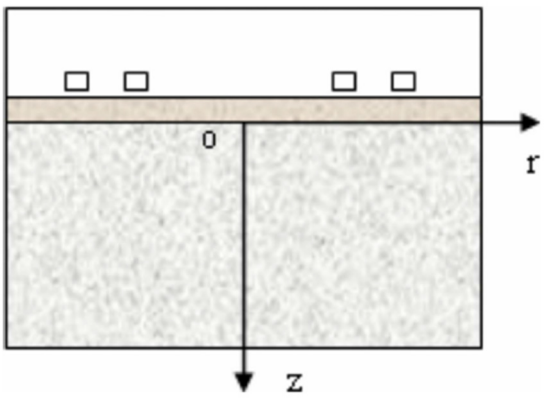

Figure 20. A schematic diagram of argon ICP chamber and the cylindrical coordinate system used in the fluid simulation with self-written code. Here, the cylindrical symmetry is utilized. The spatial size mesh numbers in the radial and axial directions are both 100, and the simulated radial and axial distances are both 10 cm. It is noted that this figure is replotted from Ref. [14] for providing the reference of understanding the data, electron mean energy and the effective source term, in Figure 21.

 doi:10.20944/preprints202604.0734.v1

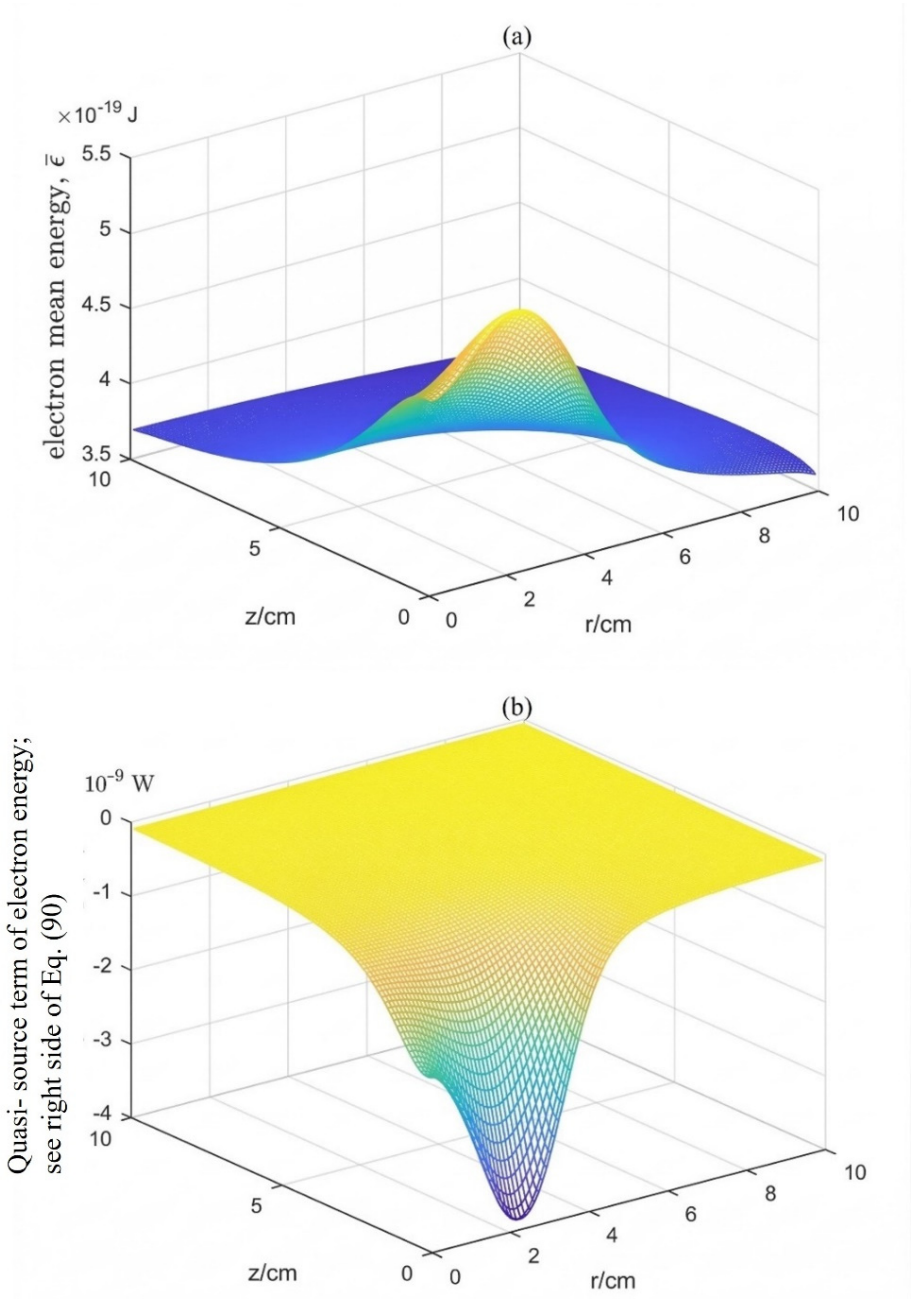

Figure 21. The electron mean energy profile (a) and (b) its effective net source in the Ar ICP, given by the fluid model simulation of self-written code. This quasi source of electron mean energy can be referred to the right side of Equation (90).

IV. Conclusions

In this article, the fluid simulations of four ICP sources, Ar/SF_6, Ar/O_2, Ar/Cl_2 and pure argon with Comsol software, and the fluid simulation of one special argon ICP source with self-written code are used to analyze the different types of self-coagulation of mass and energy. It is mentioned that the self-coagulation can be simulated and predicted by the related theory and it is always localized in the complex discharge structure. For analyzing the ions profile simulated in the low-pressure Ar/SF_6 ICP, the parabola theory in the stratified core is applied. For analyzing the ions profile in the high pressure of Ar/SF_6 ICP and the metastable profile of pure argon ICP, the ellipse theory is applied. In total, four types of self-coagulation of mass, i.e., physically ambi-polar type, chemically ambi-polar type, mono-polar type, and non-polar type, and the type of energy self-coagulation, are reported. Their implications on the activity of ambi-polar diffusion, particle physics, quantum physics, nuclear physics, microscopic species spin, and the photon models are focused on.

 doi:10.20944/preprints202604.0734.v1

References

1. Zhao, S.X. Quasi-delta negative ions density of Ar/O_2 inductively coupled plasma at very low electronegativity. *Chin. Phys. B* **2021**, *30*, 055201.
2. Zhao, S.X.; Li, J.Z. Delta distribution of electronegative plasma predicted by reformed "spring oscillator" dynamic equation with dispersion force, *Chin. Phys. B*, **2021**, *30*, 055202.
3. Tang, R.J.; Zhao, S.X.; Tian, Y. Microscopic wave dynamics and discharge structure hierarchy of highly electronegative plasma at quasi- cold ion approximation. Accepted in AIP advance.
4. Lampe, M., Manheimer, W.M., Fernsler, R.F., Slinker S.P., and Joyce G. The physical and mathematical basis of stratification in electronegative plasmas. *Plasma Sources Sci. Technol.* **2004**, *13*, 15.
5. Lichtenberg, A.J.; Vahedi, V.; Lieberman, M.A. and Rognlien T. Modeling electronegative plasma discharges. *J. Appl. Phys.* **1994**, *75*, 2339.
6. Sheridan, T.E.; Braithwaite, N.S.J.; Boswell, R.W. Relation between double layer and flux for a collisionless discharge with two negative components. *Phys. Plasmas*. **1999**, *6*, 4375.
7. Ghosh S.; Bharuthram, R. Ion acoustic solitary wave in electron-positron-ion plasma: effect of Landau damping. *Astrophys. Space Sci*. **2011**, *331*, 163.
8. Lichtenberg, A. J., Kouznetsov, I. G., Lee, Y. T., Lieberman, M. A., Kaganovich, I. D., Tsendin, L. D. Modelling plasma discharges at high electronegativity. *Plasma Sources Sci. Technol.* **1997**, *6*, 437.
9. Tang, R.J.; Zhao, S.X; Tian, Y. Discharge structure hierarchy of highly electronegative plasma and the implication on nuclear fusion at low pressure and quasi- cold ions approximation. *Adv. Theo. Comp. Phys.*, **2025**, *8*, 01.
10. Tian, Y.; Zhao, S.X. Self-coagulation theory and related comet- and semi-circle-shaped structures in electronegative and gaseous discharging plasmas in the laboratory. *Appl. Sci.* **2024**, *14*, 8041.
11. Zhao, S. X.; Tang, A. Q.; and Tian Y. Discharge structure of Ar/Cl_2 inductively coupled plasma: A cyclic study of discharge conditions at fixed power. *J. Technol. Space Plasmas*, **2025**, *1*, 218.
12. Zhao, S.X.; Tian, Y. Discharge structure theory of highly electronegative plasma and its hierarchy and interdisciplinary meanings. *AIP Adv.*, **2025**, *15*, 115028.
13. Zhao, S.X.; Xu, X.; Li, X.C.; Wang, Y.N. Fluid simulation of the E-H mode transition in inductively coupled plasma. *J. Appl. Phys.*, **2009**, *105*, 083306.
14. Gao, F.; Zhao, S.X.; Li, X.S.; Wang, Y.N. Comparison between experiment and simulation for argon inductively coupled plasma. *Phys. Plasmas*. **2009**, *16*, 113502.
15. Bukowski, J.D.; Graves, D.B.; and Vitello, P. Two-dimensional fluid model of an inductively coupled plasma with comparison to experimental spatial profiles. *J. Appl. Phys.*, **1996**, *80*, 2614.
16. Zhao, S.X. Discharge structure of Ar/SF6 inductively coupled plasma at relatively low pressures. *Glob. Open Access J. Sci.*, **2025**, *1*, 66.
17. Zhao, S.H.; Sun, Y.H. Study of transport process and discharge structure of inductively coupled electronegative plasmas via fluid model and analytic theory collaboration. *Adv. Theo. Comp. Phys.*, **2025**, *9*, 01.
18. Yukawa, H. On the nature of the mesotron. *Prog. Theo. Phys.*, **1948**, *3*, 217.
19. Monaldi, D. Life of μ : the observation of the spontaneous decay of mesotrons and its consequences. 1938-1947. *Ann. Sci.*, **2005**, *62*, 419.
20. Gorev, V.V.; Kachalov, K.O.; Serebrennikov, K.S. Oscillation spectra of isotropic electron-positron Beta (+/-) – decay plasma. *Plasma Phys. Rep.*, **1994**, *20*, 271.
21. Mukhopadhyay, B.; Singh, P. Neutrino-antineutrino asymmetry around rotating black holes. *Pramana- J. Phys.*, **2004**, *62*, 775.

 doi:10.20944/preprints202604.0734.v1

22. Tang, R.J.; Zhao, S.X.; Tian, Y. Glow discharge relative independence and hierarchy of Ar/SF_6 inductively coupled plasma sourced at high pressure and quasi-cold ions approximation. In preparation.
23. Istomin, Y.N.; Sob'yanin, D.N. Absorption of gamma-ray photons in a vacuum neutron start magnetosphere: I. Electron-positron pair production. *J. Experimental & Theo. Phys*., **2011**, *113*, 592.